Frame-Based AFDM-ISAC Waveform Design With Chirp-Enabled Pulse Compression

Qu Luo, *Member, IEEE,* Zilong Liu, *Senior Member, IEEE,* Musavian, Leila, *Member, IEEE,* Thomos, Nikolaos, *Senior Member, IEEE,* Qihao Peng, *Member, IEEE,* and Pei Xiao, *Senior Member, IEEE.*

***Abstract*—This paper proposes an Affine frequency division multiplexing (AFDM)-empowered integrated sensing and communications (ISAC) design, referred to as AFDM-ISAC. We first design a novel AFDM-ISAC frame structure that consists of both ISAC and pure data symbols. Each ISAC symbol consists of a single chirp subcarrier for both sensing and channel estimation, while the remaining subcarriers are allocated for communication. Building upon this structure, we present an analog-domain sensing receiver that down-mixes the received echo with a local chirp to fully exploit *chirp compression* gains avoiding the need for full-duplex hardware. In addition, a sensing fusion algorithm, guided by AFDM modulation parameters, is further proposed in the digital domain. Leveraging the distinct features of the proposed AFDM-ISAC frame, we present a low-complexity channel estimation scheme for high mobility channels based on a generalized complex exponential basis expansion model (GCE-BEM), along with an optimal power allocation strategy between pilot and data symbols. Moreover, to support frame-based AFDM communications, a GCE-BEM-based Kalman filter is also employed for robust intra-frame channel estimation. Simulation results demonstrate the effectiveness and superiority of the proposed schemes in terms of system flexibility, hardware complexity, and ISAC performance.**

***Index Terms*—Integrated sensing and communications (ISAC), Affine frequency division multiplexing (AFDM), single chirp subcarrier, channel estimation, generalized complex exponential basis expansion model (GCE-BEM).**

I. INTRODUCTION

LOW-altitude wireless networks (LAWNs), which interconnect aerial platforms such as unmanned aerial vehicles (UAVs), electric vertical takeoff and landing (eVTOL) aircraft, aerial robots, and other near-ground airborne nodes, have emerged as a critical enabler for future wireless communications [1], [2]. By offering flexible deployment, rapid mobility, and three-dimensional connectivity, LAWNs effectively support a wide range of applications, including emergency communications, traffic surveillance, environmental monitoring, and smart-city sensing. These applications impose a strong demand for both sensing and reliable communication services within LAWNs [3]. To meet these requirements, integrated sensing and communication (ISAC) has gained significant attention by co-designing radar and communication functionalities under a unifying wireless system [3]–[5]. Such an integration leads to improved spectral and energy efficiencies, reduced hardware and storage costs, as well as mutually enhanced sensing and communication functionalities. Among many research topics, waveforms are at the very heart of ISAC system design, attracting significant attention from both academia and industry [6], [7].

Orthogonal frequency-division multiplexing (OFDM) has been studied as one of the dominant ISAC waveforms owing to its prevalence in modern wireless systems, such as long-term evolution, 5G New Radio (NR), and Wi-Fi networks [6]. However, OFDM may suffer from significant inter-carrier interference and performance degradation in high mobility channels due to the loss of subcarrier orthogonality. Motivated by this problem, orthogonal time frequency space (OTFS) modulation was proposed, through which one can convert a time-varying multipath channel into quasi-static representations in the delay-Doppler domain [8], [9]. Another promising direction is chirp-based multicarrier waveforms, such as orthogonal chirp division multiplexing (OCDM) [10] and affine frequency division multiplexing (AFDM) [11]–[13]. In particular, AFDM generalizes OFDM and OCDM by introducing a tunable chirp rate, enabling adaptive delay-Doppler resilience and multipath separation in the affine Fourier transform (AFT) domain [14]. With this flexibility and excellent backwards-compatibility, AFDM offers a favorable trade-off between error rate performance and implementation efficiency. Importantly, AFDM is able to achieve full channel diversity with reduced pilot overhead and implementation complexity [15]. These advantages make AFDM as a promising waveform for ISAC and high-mobility LAWNs [2], [16]–[20].

A. Related Works

To date, the research on AFDM-based ISAC is still in its early stage. There are monostatic and bistatic ISAC systems, whereby the transmitter and radar receiver are co-located and spatially separated, respectively [21]. The authors in [22] investigated a bistatic sensing-aided channel estimation scheme and analyzed the ambiguity function (AF) properties of AFDM. However, their approach cannot estimate the target's velocity. Subsequently, [23] extended bistatic AFDM sensing to static target scenarios.

This work was supported in part by the UK Engineering and Physical Sciences Research Council under Grant EP/X013162/1. The work of Z. Liu, L. Musavian, and N. Thomos was supported in part by the UK Engineering and Physical Sciences Research Council under Grants EP/Y037243/1 ('TITAN/REVOL6G' and 'TITAN/LEGEND6G'), EP/X040569/1 ('HASC/RETHIN6G'), EP/X035352/1 ('DRIVE'), EP/Y000986/1 ('SORT'), and EP/X012204/1 ('PerCom'). (Corresponding author: Zilong Liu)

Qu Luo, Qihao Peng and Pei Xiao are with the 5G & 6G Innovation Centre, University of Surrey, U. K. (email: {q.u.luo, q.peng, p.xiao }@surey.ac.uk).

Zilong Liu, Musavian, Leila, Thomos, and Nikolaos are with the School of Computer Science and Electronics Engineering, University of Essex, U. K. (email: {zilong.liu,leila.musavian, nthomos}@essex.ac.uk).

Unlike [22], [23], most existing AFDM-ISAC studies focused on monostatic sensing architectures. For example, [24] introduced a matched-filter-based method combined with a fast cyclic-correlation radar algorithm to estimate target range and velocity in both time and discrete affine frequency time (DAFT) domains. Later, an improved monostatic AFDM-ISAC scheme that requires only a single AFDM symbol was proposed in [25]. After performing self-interference cancellation (SIC) in the DAFT domain, target parameters are estimated via an approximate maximum-likelihood (ML) algorithm. While the SIC mechanism effectively simplifies hardware implementation, the ML estimation remains computationally intensive due to its reliance on an exhaustive two-dimensional (2D) grid search. Unlike [24] and [25] focusing primarily on radar sensing design, [16] proposed a unified framework for joint channel estimation, data detection, and radar parameter estimation over doubly dispersive channels.

More recently, the AF and sensing performance metrics of AFDM-ISAC systems have been extensively studied in [26]–[30]. The auto- and cross-AF of AFDM chirp subcarriers were analyzed in [27], while the AF of AFDM under pulse shaped random signaling was derived in [28]. In [29], two novel metrics, i.e., sensing spectral efficiency (SE) and sensing outage probability, were introduced to characterize the sensing communication trade-offs. Closed-form expressions for the Cramér–Rao lower bounds (CRLBs) and the AF for pilot-assisted AFDM waveforms were further derived in [31]. In addition, the authors in [30] derived a closed-form expression for the AF of AFDM waveforms modulated with M-ary quadrature amplitude modulation (QAM) and identified a chirp-rate condition that minimizes sidelobe levels in the delay/range domain. While the above works primarily focused on target parameter estimation (e.g., range and velocity), an AFDM-ISAC framework that estimates the multipath power–delay profile to enhance communication performance was proposed in [32]. Furthermore, in contrast to prior studies such as [22]–[25], [29]–[33], which mainly considered far-field targets, a joint angle-delay-Doppler estimation scheme for AFDM-ISAC systems operating in mixed near-field and far-field environments was developed in [34].

B. Motivations and Contributions

One critical challenge in monostatic ISAC system design is that SIC is often overlooked [25]. Since the transmitter and receiver are co-located, the transmit waveform may leak into the receive chain, causing severe self-interference and posing a major barrier to practical monostatic radar implementations. Note that most AFDM- and OTFS-based ISAC designs adopt a communication-centric architecture by largely reusing the communication processing chain [23], [24], [29], [31], [32], [35], [36]. Such designs rely on the strong assumption of ideal SIC, which in turn requires costly full-duplex interference cancellation techniques. Additionally, while chirp signals are well known for their *pulse compression* capability and hence are widely used in conventional radar systems, this advantage has yet to be fully exploited in AFDM-based ISAC designs, despite some preliminary attempts in [25]. Although there are many works on AFDM in recent years, limited work is done on AFDM frame structure which is a key step for its practical applications, especially for its applications in ISAC. Furthermore, conventional channel estimation approaches for doubly selective channels are tedious and suffer from significant training overhead, thus leading to significant compromise of SE. Against these challenges, this paper investigates a frame-based AFDM-ISAC scheme in terms of sensing and channel estimation.

The main contributions of this paper are summarized as follows:

- We first propose a novel AFDM-ISAC frame structure composed of ISAC symbols and pure data symbols. In each ISAC symbol, a single subcarrier is dedicated as the sensing and pilot subcarrier (SPS), while the remaining subcarriers are allocated for communication purpose or used as guard bands. Since the SPS sweeps the entire AFDM bandwidth, it preserves the range resolution equivalent to that of a full AFDM symbol. The received echo of the SPS, together with the interference introduced by the data subcarriers are then analyzed in detail.
- We further introduce a dedicated analog-domain sensing receiver, equipped with a judiciously designed low-pass filter (LPF). We show that the interference from the data subcarriers can be well suppressed, thereby eliminating the need for a complex and costly full-duplex design. By placing the analog-to-digital converter (ADC) after the LPF, saturation caused by transmitter leakage can be alleviated, since the LPF suppresses high-frequency leakage components before digitization. In addition, an AFDM modulation parameter, i.e., chirp slop, oriented sensing processing algorithm is proposed. We show that the proposed AFDM-ISAC frame can flexibly balance sensing and communication requirements, such as the sensing performance, the maximum sensing range and speed, communication efficiency, and communication performance.
- Building upon the proposed AFDM-ISAC frame structure, a generalized complex exponential basis expansion model (GCE-BEM) is used to approximate the time varying channels, thus achieving accurate channel estimation with reduced computational complexity. We derive the signal-to-interference-plus-noise ratio (SINR) of the GCE-BEM-assisted channel estimation to guide the power allocation between the pilot and data subcarriers. Furthermore, to address the channel variations of the proposed AFDM-ISAC signaling, a Kalman filter based exponential basis expansion model (KF-BEM) is proposed for efficient channel tracking.
- We conduct extensive simulation results to demonstrate the sensing and communication superiority of the proposed AFDM-ISAC. We show that the proposed AFDM-ISAC solutions outperform the conventional OTFS-, OFDM- and AFDM-based schemes in terms of the range and speed root mean square error (RMSE). It is shown that selecting AFDM parameter $c_1 \in \left\{\frac{2}{2N}, \frac{3}{2N}, \frac{4}{2N}\right\}$, along with a pure-data-to-ISAC symbol ratio $\eta \in$

$\{1,2,3\}$, yields a desirable trade-off between sensing accuracy and communication performance.

The remainder of this paper is outlined as follows. Section II introduces the basic AFDM principles. The proposed AFDM-ISAC frame structure design is introduced in Section III. Section IV and Section V present the proposed sensing and communication receiver design, respectively. Section VI evaluates the sensing and communication performance of the proposed AFDM-ISAC, followed by the conclusions in Section VII.

C. Notation

$\mathbb{C}^{k\times n}$ denotes the $(k\times n)$-dimensional complex matrix. $\mathbf{I}_n$ denotes an $n\times n$-dimensional identity matrix. $\mathrm{diag}(\mathbf{x})$ gives a diagonal matrix with the diagonal vector of $\mathbf{x}$. $(\cdot)^{\mathcal{T}}$, $(\cdot)^{\dagger}$ and $(\cdot)^{\mathcal{H}}$ denote the transpose, the conjugate and the Hermitian transpose operation, respectively. $\|\mathbf{x}\|_2$ and $|x|$ return the Euclidean norm of vector $\mathbf{x}$ and the absolute value of x, respectively. $\mathbb{C}$ and $\mathbb{Z}$ denote the complex and integer spaces, respectively. $\langle\cdot\rangle_N$ denotes the modulo-N operation, and $\mathcal{CN}(0,1)$ denotes the complex distribution with zero mean and unit variance.

II. INTRODUCTION TO BASIC PRINCIPLES OF AFDM

This section introduces the time–frequency representation and provides a detailed mathematical formulation of AFDM subcarriers, which serves as the foundation for the proposed AFDM-ISAC design. The AFDM subcarriers are constructed based on the AFT, whose kernel is defined as [11]

$$K_{a,b,c,d}(t,u)=\frac{1}{\sqrt{2\pi|b|}}\mathrm{e}^{-j\left(\frac{a}{2b}u^2+\frac{1}{b}ut+\frac{d}{2b}t^2\right)},\tag{1}$$

where (a,b,c,d) are the AFT parameters and t and u denote the time- and affine-domain variables, respectively. By sampling the transform kernel at the AFT domain with a sample interval Δu, one has

$$K_{a,b,c,d}(t,u)|_{u=n\Delta u}=\frac{1}{\sqrt{2\pi|b|}}\mathrm{e}^{j\left(\frac{a}{2b}n^2\Delta u^2+\frac{1}{b}n\Delta ut+\frac{d}{2b}t^2\right)}.\tag{2}$$

Let $\Delta t = T/N$ denote the sampling interval in the time domain, where T is the signal duration and N the total number of samples. Following [11], the AFDM modulation parameters are defined as $c_1=\frac{d}{4\pi b}\Delta t^2$ and $c_2=\frac{a}{4\pi b}\Delta u^2$. The transform is reversible if $\Delta t\Delta u=\frac{2\pi|b|}{N}$ holds [11]. The AFDM defined in [11] uses the first type as the transform kernel. To align with the signal model in [11], we consider $b>0$ as well. Under the constraints of $\Delta t\Delta u=\frac{2\pi|b|}{N}$ and $b>0$, (2) reduces to

$$K_n(t)=\mathrm{e}^{j2\pi\left(\frac{c_1N^2}{T^2}t^2+\frac{nt}{T}+c_2n^2\right)},b>0,\tag{3}$$

which forms a set of N orthogonal chirp signals, i.e., $\{K_n(t)\}_{n=0}^{N-1}$.

After sampling $K_n(t)$ with period Δt, the AFT kernel in the digital domain can be expressed as

$$\Psi_n(m)=\frac{1}{\sqrt{N}}e^{j2\pi\left(c_1m^2+c_2n^2+\frac{nm}{N}\right)}.\tag{4}$$

By collecting N normalized samples of each signal in (4), we can obtain the so-called DAFT matrix. Namely, $\mathbf{A}=\Lambda_{c_2}\mathbf{F}\Lambda_{c_1}$ with $\Lambda_c=\mathrm{diag}\left(e^{-j2\pi cn^2},n=0,1,\ldots,N-1\right)$, where $\mathbf{F}$ denotes the $N\times N$ DFT matrix with entries $[\mathbf{F}]_{m,n}=e^{-j2\pi mn/N}/\sqrt{N}$.

Remark 1: Let $B=\frac{1}{\Delta t}=\frac{N}{T}$. *It should be noted that* $K_n(t), 0\le n\le N-1$, *occupies a bandwidth of* $2c_1NB$ *within the time duration* T. *However, according to the sampling theorem, time-domain sampling introduces spectral wrapping in the digital AFDM signal, thereby limiting the effective bandwidth to the range* $[-0.5B, 0.5B]$. *Fig. 1(a) illustrates an example of the wrapped time–frequency representation with* $c_1=\frac{1}{N}$.

In the sequel, we derive the detailed expressions of the time-domain wrapped AFDM subcarriers. Define $\phi_n(t)=\frac{c_1N^2}{T^2}t^2+\frac{nt}{N}B$, whose derivative with respect to t is $\phi_n^{'}(t)=\frac{2c_1N^2}{T^2}t+\frac{n}{N}B$. Note that $\phi_n(t)$ describes the phase changes of the $K_n(t)$ with $\phi_n^{'}(t)$ being the changing rate. Then, the wrapped AFDM subcarriers can be expressed as

$$\Psi_n(t)=\mathrm{e}^{j2\pi\left(\int_0^t\bar{\phi}_n^{'}(x)dx+c_2n^2\right)},\tag{5}$$

where $\bar{\phi}_n^{'}(x)=\left\langle\phi_n^{'}(x)+\frac{B}{2}\right\rangle_B-\frac{B}{2}$. Later, we will show that by judiciously aggregating the wrapped AFDM subcarriers, it enables enhanced range and velocity estimation.

Remark 2: The OCDM system [10] defines time-domain chirp subcarriers as $K_n(t)=e^{-j\pi/4}\mathrm{e}^{-j\pi\frac{N}{T^2}\left(t-\frac{T}{N}n\right)^2}$. *In fact, for* $c_1=c_2=-1/2N$ *and* $b>0$, *(3) simplifies to*

$$K_n(t)=\mathrm{e}^{-j2\pi\left(\frac{n^2}{2N}-\frac{nt}{T}+\frac{N}{2T^2}t^2\right)}=\mathrm{e}^{-j\pi\frac{N}{T^2}\left(t-\frac{T}{N}n\right)^2},\tag{6}$$

which is essentially equivalent to the OCDM subcarriers in [10], except for a fixed phase shift $e^{-j\pi/4}$.

III. THE PROPOSED AFDM-ISAC SIGNAL STRUCTURE

In this section, we first introduce the proposed AFDM-ISAC frame structure. We then proceed to describe the sensing and communication signal models.

A. The Proposed AFDM-ISAC Signal Model

The proposed AFDM-ISAC frame structure is illustrated in Fig. 1(b). It consists of ISAC symbols and pure data symbols. An ISAC symbol is employed for both sensing and communication, whereas a data symbol is dedicated solely to communication. Each frame contains N_{s} ISAC symbols, which are periodically placed at positions of

$$\mathcal{I}_{\mathrm{ISAC}}=\{0,\eta+1,\ldots,(N_{\mathrm{s}}-1)(\eta+1)\},\tag{7}$$

where $\eta\in\mathbb{Z}$ denotes the ratio of pure-data symbols to ISAC symbols. Therefore, η controls the trade-off between the number of ISAC and data symbols. In particular, when $\eta=0$, the AFDM-ISAC frame only consists of ISAC symbols. Accordingly, the total number of AFDM symbols is given by $N_F=(1+\eta)N_{\mathrm{s}}$.

As shown in Fig. 1(b), each ISAC symbol contains sensing and channel estimation subcarriers, communication subcarriers, and guard subcarriers. The $(N/2)$th subcarrier, $\Psi^{k}_{\frac{N}{2}}(t)$, is designated as the SPS. The reasons are twofold: 1) Since each AFDM subcarrier spans the entire bandwidth, using a

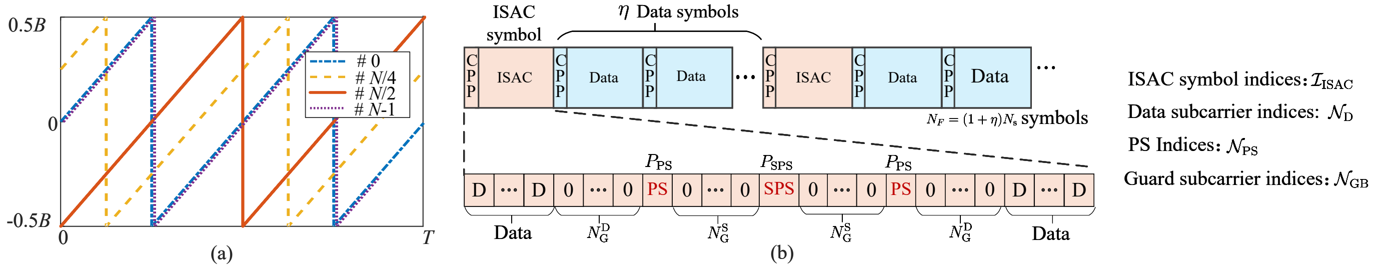

(a) (b)

Fig. 1: Illustration of (a) wrapped AFDM subcarriers ($K = 2$) and (b) the proposed AFDM-ISAC frame structure.

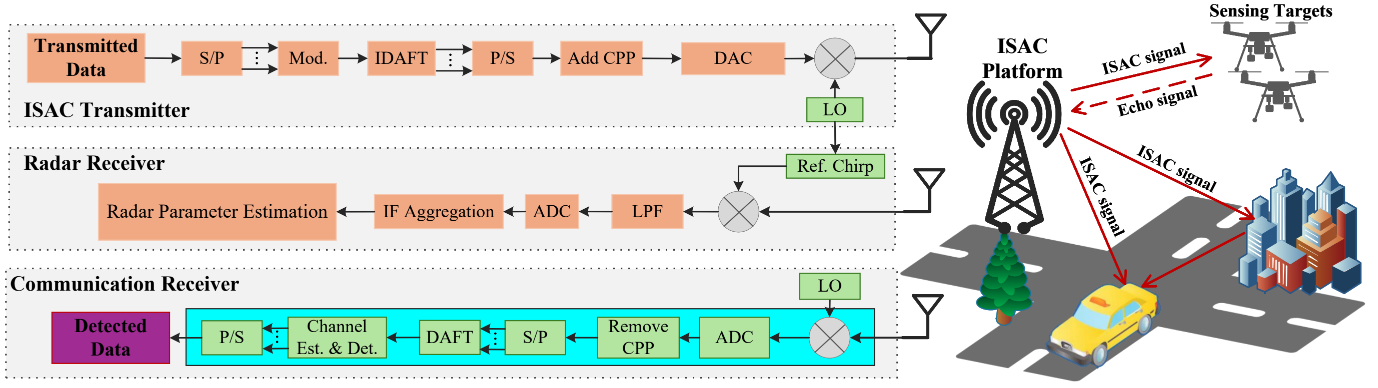

Fig. 2: The proposed AFDM-ISAC signal processing.

single chirp subcarrier for sensing can still preserve the sensing resolution. Later, we will show that the proposed design also leads to a low-complexity sensing receiver and improved communication SE; 2) According to Remark 1, the $(N/2)$th AFDM subcarrier starts from $-0.5B$ and sweeps the full bandwidth K times for $c_1 = \frac{K}{2N}$ with $K \in \mathbb{Z}$. For dechirping-based sensing receiver design, continuous chirp signals are desired. To further improve channel estimation accuracy, two additional pilot subcarriers (PS) are also inserted. Although a single subcarrier can capture the entire channel in AFDM, it relies on a large c_1 value to ensure that multipaths with fractional Doppler are well separated in the DAFT domain for accurate estimation [37]. Hence, we adopt a multiple-pilot structure to mitigate the interference caused by fractional Doppler across different paths. It is also worth noting that the communication pilot guard is much shorter than the sensing guard. To further reduce the number of channel parameters to be estimated, the BEM model will be introduced in Section VI. In addition, guard-band subcarriers are placed to suppress interference. Let $N_{\mathrm{G}}^{\mathrm{S}}$ and $N_{\mathrm{G}}^{\mathrm{D}}$ denote the numbers of guard subcarriers between the SPS and PS, and between the PS and data subcarriers, respectively. The number of communication subcarriers in each ISAC symbol is then given by

$$N_{\mathrm{C}} = N - 2N_{\mathrm{G}}^{\mathrm{D}} - 2N_{\mathrm{G}}^{\mathrm{S}} - 3. \tag{8}$$

The modulated data of the ith symbol, $i \in \mathcal{I}_{\mathrm{ISAC}}$, in the DAFT domain is given by

$$x_{i,n} = \begin{cases} \sqrt{P_{\mathrm{SPS}}}, & n = \frac{N}{2}, \\ \sqrt{P_{\mathrm{PS}}}, & n \in \mathcal{N}_{\mathrm{PS}} \\ 0, & n \in \mathcal{N}_{\mathrm{GB}}, \\ \text{Data Symbols}, & n \in \mathcal{N}_{\mathrm{D}}, \end{cases} \tag{9}$$

where P_{SPS} and P_{PS} are the allocated power levels for the SPS and PS, respectively, and $\mathcal{N}_{\mathrm{PS}} = \{\frac{N}{2} - N_{\mathrm{G}}^{\mathrm{D}} - N_{\mathrm{G}}^{\mathrm{S}} - 1, \frac{N}{2} + N_{\mathrm{G}}^{\mathrm{D}} + N_{\mathrm{G}}^{\mathrm{S}} + 1\}$, $\mathcal{N}_{\mathrm{GB}}$ and $\mathcal{N}_{\mathrm{D}}$ are the indices of the PS, guard band, and data subcarriers, respectively. Accordingly, the continuous-time waveform of the ith symbol can be expressed as

$$s_i(t) = \sum_{n=0}^{N-1} x_{i,n} \Psi_n(t - iT). \tag{10}$$

This waveform is transmitted after adding cyclic prefix (CP). For digital transmission, the time-domain signal in the ith symbol is expressed as $\mathbf{s}_i = \mathbf{A}^{\mathcal{H}} \mathbf{x}_i \in \mathbb{C}^{N\times 1}$, where $\mathbf{x}_i = [x_{i,0}, x_{i,1}, \ldots, x_{i,N-1}]^{\mathcal{T}}$. Owing to the distinct signal periodicity, a chirp-periodic prefix (CPP) is employed in the digital domain, i.e., [38]

$$s_i[n] = s_i[N+n]e^{-j2\pi c_1(N^2+2Nn)}, n = -N_{\mathrm{CPP}}, \cdots, -1, \tag{11}$$

where N_{CPP} denotes the CPP length. For $c_1 = \frac{K}{2N}$ with $K \in \mathbb{Z}$, the CPP reduces to the conventional CP.

B. Sensing Signal Model

Let L be the number of sensing targets, with R_l and v_l denoting the range and velocity of the lth target, respectively. The received echo signal of the lth target has the same form as $s_i(t)$ but with a delay τ_l, defined as [1]

$$\tau_l = 2(R_l + v_l t)/\nu, \tag{12}$$

where ν denotes the speed of light. Similar to existing works, we assume line-of-sight propagation [22]–[25], [29]–[33], which is also the predominant channel model for aerial UAV scenarios. Accordingly, the received echo can be expressed as

$$r_i(t) = \sum_{l=0}^{L-1} h_l^{\mathrm{S}} s_i(t - \tau_l) e^{j2\pi f_c (t-\tau_l)} + w_i(t), \tag{13}$$

---

[1] It is worth noting that this delay model effectively characterizes both delay and Doppler effects.

where h_l denotes the channel gain of the lth target, $w_i(t) \sim \mathcal{CN}(0, \sigma_s)$, and f_c is the carrier frequency. Note that h_l accounts for both channel attenuation and radar cross-section attenuation [21].

C. Communication Signal Model

We consider a doubly selective channel between the ISAC platform and the communication user. For simplicity, its equivalent discrete channel impulse response is adopted, with the expression at time index n and tap p of the ith AFDM symbol given by

$$h_i(n,p) = \sum_{p=0}^{P-1} h_{i,p} e^{-j2\pi f_{i,p} n} \delta(p - p_i), \tag{14}$$

where P is the number of paths, $h_{i,p}$ and $f_{i,p}$ denote the channel fading coefficient and Doppler shift of the pth path in the ith AFDM symbol, respectively. Due to user mobility, the physical channel taps are time-varying. By assuming a channel taps remain unchanged within a given AFDM symbol but vary across different symbols. Let $\mathbf{h}_i = [h_{i,1}, h_{i,2}, \ldots, h_{i,P}]^{\mathcal{T}}$. According to the wide-sense stationary uncorrelated scattering model, the time-varying $\mathbf{h}_i$ can be approximated by a first-order auto regression (AR) model [39], [40].

$$\mathbf{h}_{i+1} = \widetilde{\mathbf{S}}\mathbf{h}_i + \widetilde{\mathbf{v}}_i, \tag{15}$$

where $\widetilde{\mathbf{S}} \in \mathbb{C}^{P \times P}$ denotes the state transition matrix which is at the receiver [40], and $\widetilde{\mathbf{v}}_i \in \mathcal{CN}(\mathbf{0}, \sigma_v \mathbf{I}_P)$.

Note that (14) can be expressed in matrix form as

$$\mathbf{H}_i = \begin{bmatrix} h_i(0,0) & 0 & \cdots & h_i(0,P-1) & \cdots & h_i(0,1) \\ h_i(1,1) & h_i(1,0) & 0 & \cdots & \cdots & h_i(1,2) \\ \vdots & \ddots & \ddots & \ddots & \ddots & \vdots \\ 0 & \cdots & 0 & h_i(N-1,P-1) & \cdots & h_i(N-1,0) \end{bmatrix}. \tag{16}$$

Then, the received signal of the ith AFDM symbol in the discrete AFT domain is given by

$$\mathbf{y}_i = \mathbf{A}\mathbf{H}_i\mathbf{A}^{\mathcal{H}}\mathbf{x}_i + \mathbf{n}_i \triangleq \mathbf{H}_{\text{eff},i}\mathbf{x}_i + \mathbf{n}_i, \tag{17}$$

where $\mathbf{n}_i \in \mathcal{CN}(0, \sigma_c \mathbf{I}_N)$ denotes the Gaussian noise and $\mathbf{H}_{\text{eff},i} = \mathbf{A}\mathbf{H}_i\mathbf{A}^{\mathcal{H}}$ denotes the effective channel matrix.

IV. THE PROPOSED SENSING RECEIVER DESIGN

Building upon the aforementioned AFDM-ISAC signal model, this section presents a novel sensing receiver, including the analog-domain sensing process and the digital-domain parameter estimations, as shown in Fig. 2. Finally, the detailed performance indicators are presented. Since only the ISAC symbols are relevant to the sensing receiver, we reuse the subscript i in this section to denote the index of the ith ISAC symbol, i.e., $i \in \{0, 1, \ldots, N_{\text{s}} - 1\}$.

A. Sensing Process

We denote t_s as the start time of the ith ISAC symbol and re-define t as follows:

$$t = iT_{\text{s}} + t_s, \quad 0 \le t_s < T, \quad 0 \le i \le N_s - 1, \tag{18}$$

where $T_{\text{s}} = (1+\eta)(T + T_{\text{CPP}})$, with $T_{\text{CPP}} \triangleq \frac{TN_{\text{CPP}}}{N}$ denoting the CPP duration. By substituting (18) into (12), we obtain

$$\tau_l = \frac{2(R_l + v_l(iT_{\text{s}} + t_s))}{\nu}. \tag{19}$$

Accordingly, based on (13), the received echoes of the N_F symbols can be expressed as

$$r(t) = \sum_{i=0}^{N_{\text{F}}-1} \sum_{l=0}^{L-1} h_l^{\text{S}} s_i(t - \tau_l) e^{j2\pi f_c (t-\tau_l)} + w(t). \tag{20}$$

On the other hand, the chirp synthesizer of the radar receiver, which shares the same local oscillator (LO) with the AFDM-ISAC transmitter, generates the conjugated version of the SPS as the reference chirp. A delay is introduced to this local reference signal for sensing purpose. Specifically, the ith reference signal generated by the chirp synthesizer from the $N/2$-th conjugated AFDM SPS is expressed as

$$s_{\text{ref},i}(t_s - \tau_{\text{ref}}) = \Psi^*_{\frac{N}{2}}\left(t_s - \tau_{\text{ref}}\right) e^{-j2\pi f_c (t_s - \tau_{\text{ref}})}, \tag{21}$$

where $\tau_{\text{ref}} = \frac{2R_{\text{ref}}}{\nu}$, with R_{ref} denoting the sensing range of interest. The parameter R_{ref} will be discussed in more detail later. Upon receiving the echo signal, $r(t)$ is mixed with $s_{\text{ref},i}(t)$ to generate the intermediate-frequency (IF) signal, i.e.,

$$\begin{aligned} & r_i^{\text{IF},l}(t)|_{t=iT_{\text{s}}+t_s} = r_i(t) s_{\text{ref},i}(t - \tau_{\text{ref}}) \\ & \simeq \underbrace{\sum_{l=1}^{L} \sqrt{P_{\text{SPS}}} h_l^{\text{S}} \Psi_{\frac{N}{2}}(t - \tau_l - iT_{\text{s}}) \Psi^*_{N/2}(t - \tau_{\text{ref}} - iT_{\text{s}}) e^{-j2\pi f_c (\tau_l - \tau_{\text{ref}})}}_{\text{Desired IF signal}} \\ & + Z^{\text{IF}}(t), \end{aligned} \tag{22}$$

where

$$\begin{aligned} Z^{\text{IF}}(t) = \sum_{l=1}^{L} \sum_{n \in \{\mathcal{N} \setminus \frac{N}{2}\}} & h_l^{\text{S}} x_{i,n} \Psi_n(t - \tau_l - iT_{\text{s}}) \\ & \Psi^*_{N/2}(t - iT_{\text{s}}) e^{-j2\pi f_c (\tau_l - \tau_{\text{ref}})} + \widetilde{w}(t), \end{aligned} \tag{23}$$

denotes the interference from other chirp subcarriers, $\widetilde{w}(t) = s_{\text{ref},i}(t_s - \tau_{\text{ref}}) w(t)$ and $\mathcal{N} \setminus \frac{N}{2}$ denotes the set of N subcarriers by excluding the SPS. As mentioned earlier, the SPS sweeps the bandwidth K times. Based on (5), the kth sweeping component of the SPS, denoted by $\Psi^k_{\frac{N}{2}}(t)$, can be expressed as

$$\Psi^k_{\frac{N}{2}}(t) = e^{j2\pi\left(\frac{\alpha}{2}t^2 - \left(\frac{1}{2}+k\right)Bt + \frac{N^2}{4}c_2\right)}, k \in \{0, 1, \ldots, K\}, \tag{24}$$

where $\alpha \triangleq \frac{c_1 B}{2T}$ is the chirp rate.

Next, we focus on analyzing the desired IF signal. In the case of $\tau_l > \tau_{\text{ref}}, \forall l$, Fig. 3 illustrates an example of the time–frequency representation of the transmitted SPS and the received echo with $c_1 = \frac{1}{N}$. We categorize the symbol duration into three types of time windows, i.e.,

$$\begin{cases} \mathcal{T}_k^{\text{I}} = \left\{ t_s | t_s \in \left[\frac{kT_{\text{s}}}{K} + \tau, \frac{(k+1)T}{K} + \tau_{\text{ref}} \right] \right\}, & k = 0, \cdots, K-1 \\ \mathcal{T}_k^{\text{II}} = \left\{ t_s | t_s \in \left(\frac{(k+1)T}{K} + \tau_{\text{ref}}, \frac{(k+1)T}{K} + \tau \right] \right\}, & k = 0, \cdots, K-2 \\ \mathcal{T}_k^{\text{III}} = \left\{ t_s | \text{otherwise} \right\}. \end{cases} \tag{25}$$

By substituting (24) into (22), the IF signal from mixing the kth SPS echo component of the lth target with the reference $s_{\text{ref},i}(t)$ is given by

$$\begin{aligned}
&\Psi^{k}_{N/2}(t_s-\tau_l)e^{j2\pi f_c(t_s-\tau_l)}s_{\text{ref},i}(t-\tau_{\text{ref}})\big|_{t_s\in\mathcal{T}^{\text{I}}_c}\\
&=\Psi^{c}_{N/2}(t_s-\tau_l)\Psi^{k,*}_{N/2}(t_s-\tau_{\text{ref}})e^{-2\pi f_c(\tau_l-\tau_{\text{ref}})}\\
&=e^{-j2\pi\left(-\frac{\alpha}{2}\left(\tau_l^2-\tau_{\text{ref}}^2\right)+\alpha t_s(\tau_l-\tau_{\text{ref}})+\left(f_c-\left(\frac{1}{2}+k\right)B\right)(\tau_l-\tau_{\text{ref}})\right)}\\
&\overset{\text{(i)}}{\simeq}e^{-j2\pi\left(\alpha t_s(\tau_l-\tau_{\text{ref}})+\left(f_c-\left(\frac{1}{2}+k\right)B\right)(\tau_l-\tau_{\text{ref}})\right)}\\
&\overset{\text{(ii)}}{\simeq}\underbrace{e^{-j2\pi\left(\frac{2\alpha\Delta R_l}{\nu}+\frac{2v_l}{\nu}\left(f_c-\left(\frac{1}{2}+k\right)B+\alpha iT_{\text{s}}\right)\right)t_s}}_{\text{Beat frequency}}\\
&\quad\underbrace{e^{\frac{-j4\pi v_l\left(f_c-\left(\frac{1}{2}+k\right)B\right)}{\nu}iT_{\text{s}}}}_{\text{Phase change over each symbol}}\underbrace{e^{\frac{-j4\pi\Delta R_l\left(f_c-\left(\frac{1}{2}+k\right)B\right)}{\nu}+\frac{-j4\pi\alpha v_l t_s^2}{\nu}}}_{\text{Phase}},
\end{aligned}\tag{26}$$

where $t_s\in\mathcal{T}^{\text{I}}_k$. Step (i) holds due to the fact that $-\frac{\alpha}{2}(\tau_l^2-\tau_{\text{ref}}^2)$ is relatively small and can therefore be neglected. Step (ii) follows by substituting τ with (12), where $\Delta R_l=R_l-R_{\text{ref}}$[2]. In addition, in (26), the term $\frac{-j4\pi\alpha v_l t_s^2}{\nu}$ is also small and can be neglected. Hence, the final phase of the desired IF signal at the kth component can be expressed as

$$\begin{aligned}
\text{IF}^{k}_{\frac{N}{2},i}(t_s)&=\phi_0^k+f_d^k iT_{\text{s}}+\text{BF}^{k}_{\frac{N}{2},i}t_s,t_s\in\mathcal{T}^{\text{I}}_k,\\
f_d^k&=\frac{2v_l\left(f_c-\left(\frac{1}{2}+k\right)B\right)}{\nu},\\
\text{BF}^{k}_{\frac{N}{2},i}&=\frac{2\alpha\Delta R_l}{\nu}+\frac{2v_l}{\nu}\left(f_c-\left(\frac{1}{2}+k\right)B+\alpha iT_{\text{s}}\right),\\
\phi_0^k&=\frac{2\Delta R_l\left(f_c-\left(\frac{1}{2}+k\right)B\right)}{\nu},
\end{aligned}\tag{27}$$

where f_d^k and $\text{BF}^{k}_{\frac{N}{2},i}$ denote the Doppler and BF terms, respectively, and ϕ_0^k represents the initial phase obtained by neglecting the term $-j4\pi\alpha v_l t_s^2/\nu$ due to its insignificance. Similarly, a mixed signal for the wrapped components, i.e., $t_s\in\mathcal{T}^{\text{II}}_c$, can be readily obtained. Specifically, the IF signal has the same form as (27) but with different IF values and initial phases respectively given by

$$\begin{aligned}
\overline{\text{BF}}^{k}_{\frac{N}{2},i}&=\text{BF}^{k}_{\frac{N}{2},i}-B,\\
\overline{\phi}_0^k&=2\Delta R_l\Big(f_c-\Big(\frac{3}{2}+k\Big)B\Big)/\nu.
\end{aligned}\tag{28}$$

Note that (27) is obtained by choosing t_s as the common reference start time for all K chirp segments within each ISAC symbol. Since each chirp segment physically starts at a different time instant, we define t_s^k as the local start time of the kth chirp segment, i.e.,

$$t_s^k\triangleq t_s-\frac{kT}{K},\quad 0\le t_s^k<\frac{T}{K},\tag{29}$$

which measures the elapsed time from the beginning of the kth segment. Substituting (29) into (27) and utilizing the identity $\alpha\frac{T}{K}=B$, the IF signal in (27) can be equivalently rewritten as

$$\text{IF}^{k}_{\frac{N}{2},i}(t_s^k)=\phi_0^0+f_d^0 iT_{\text{s}}+\text{BF}^{0}_{\frac{N}{2},i}t_s^k.\tag{30}$$

As shown in (30), by adopting the time reference t_s^k, the Doppler, BF, and initial phase are inherently independent of the chirp-sweep index k. This property motivates the proposed AFDM-oriented parameter estimation presented in Section IV-C.

B. LPF Design

It should be noted that the noise term $Z^{\text{LF}}(t)$ in (22) may not be Gaussian; instead, it has a similar form to that of (26). Specifically, $\Psi_n(t-\tau_l-iT_{\text{s}})\Psi_{N/2}(t-iT_{\text{s}}),n\in\mathcal{N}_{\text{D}}\cup N_{\text{PS}}$, exhibits an IF signal similar to (26) but with a different BF. This indicates that $Z^{\text{LF}}(t)$ can be effectively suppressed by properly designing a LPF and selecting a suitable guard band. In the following, we present the BF of the PS chirp subcarrier. The BF of the left PS mixed with the SPS, i.e., the BF of $\Psi_{\frac{N}{2}-N_{\text{G}}^{\text{S}}-1}(t-\tau_{\text{ref}}-\tau_l-iT_{\text{s}})s_{\text{ref},m}(t-\tau_{\text{ref}}-iT_{\text{s}})$, can be expressed as

$$\text{BF}_{\frac{N}{2}-N_{\text{G}}^{\text{S}}-1}\in\Big\{\frac{2\alpha\Delta R_l}{\nu}-N_{\text{G}}^{\text{S}}\Delta f,\frac{2\alpha\Delta R_l}{\nu}-N_{\text{G}}^{\text{S}}\Delta f+B\Big\}.\tag{31}$$

Similarly, the BF of the right PS mixed with the SPS can be expressed as

$$\text{BF}_{\frac{N}{2}+N_{\text{G}}^{\text{S}}+1}\in\Big\{\frac{2\alpha\Delta R_l}{\nu}+N_{\text{G}}^{\text{S}}\Delta f,\frac{2\alpha\Delta R_l}{\nu}+N_{\text{G}}^{\text{S}}\Delta f-B\Big\}.\tag{32}$$

In addition, since the PSs are the closest nonzero chirp subcarriers to the SPS, it can be readily verified that the BF of the nth communication subcarrier is lower bounded by

$$\text{BF}_n\ge\min\Big\{\text{BF}_{\frac{N}{2}-N_{\text{G}}^{\text{S}}-1},\text{BF}_{\frac{N}{2}+N_{\text{G}}^{\text{S}}+1}\Big\},\forall n\in\mathcal{N}\backslash\frac{N}{2}.\tag{33}$$

The LPF should be designed to pass the desired IF signal while suppressing unnecessary high-frequency interference as well as the IF signals from communication subcarriers. Denote f_{stop} and f_{pass} as the stopband and passband of the LPF, respectively. Hence, we have

$$\begin{aligned}
f_{\text{pass}}&\ge\text{BF}_{\frac{N}{2},\max}\equiv\frac{2\alpha|\Delta R_{\max}|}{\nu},\\
f_{\text{stop}}&\le N_{\text{G}}^{\text{S}}\Delta f-\frac{2\alpha|\Delta R_{\max}|}{\nu},
\end{aligned}\tag{34}$$

where $\text{BF}_{\frac{N}{2},\max}$ denotes the maximum BF of the desired IF signal, and $\Delta R_{\max}=\max\limits_{l}(R_l-R_{\text{ref}})$ represents the maximum distance of the sensing targets of interest. In addition, the maximum BF of the desired IF signal must satisfy

$$\frac{2|\Delta R_{\max}|}{\nu}<\frac{N_{\text{G}}^{\text{S}}T}{N}.\tag{35}$$

Thus, there is no mis-mixing between the SPS and PS. From (35), the maximum detectable range can be extended by: 1) increasing the guard-band size N_{G}^{S}, 2) reducing Δf, and 3) selecting a reference distance R_{ref} closer to the region of interest. In fact, R_{ref} serves the midpoint of the sensing window, and the proposed system can detect targets within $\left(R_{\text{ref}}-\frac{\nu N_{\text{G}}^{\text{S}}T}{2N},R_{\text{ref}}+\frac{\nu N_{\text{G}}^{\text{S}}T}{2N}\right)$.

Remark 3: For monostatic sensing, in the presence of on-board leakage from the ISAC transmitter, mixing the SPS with its local reference produces a direct current component, whereas the other subcarriers generate IF components at much higher BFs that can be effectively suppressed by the LPF. By placing the ADC after the LPF, saturation induced

---

[2] The beat frequency (BF) in (26) refers to the frequency component of the IF signal that carries the target range information. By estimating the BF, the target range can be determined.

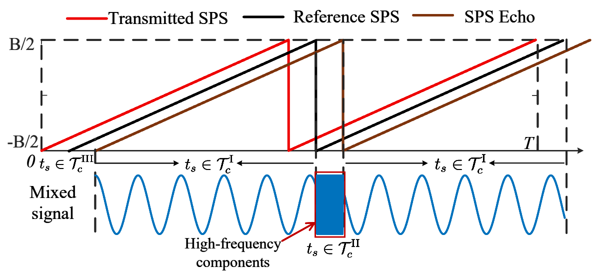

Fig. 3: Illustration of the transmitted SPS, the corresponding received echo, and the IF signal with $K = 2$.

by transmitter leakage can be mitigated, thereby eliminating the need for a complex and costly full-duplex design. Also, since the ISAC transmitter and radar receiver are co-located and share the same LO, carrier frequency synchronization is inherently guaranteed and the correlated phase noise is largely canceled during the dechirping process.

Remark 4: As the maximum BF of the desired IF signal is significantly lower than the bandwidth, i.e., $BF_{\frac{N}{2},max} \ll B$, the ADC sampling rate can be substantially reduced relative to the original signal bandwidth, thereby lowering the hardware complexity. Compared to conventional communication-centric sensing receivers that require a wideband ADC with sampling rate $\geq B$, full-duplex SIC, and digital-domain matched filtering over the entire signal bandwidth, the proposed receiver relies only on a low-cost analog mixer, an LPF, and a narrowband ADC, achieving a substantial reduction in both hardware cost and computational complexity.

C. *AFDM Parameter-Oriented Estimation*

After the LPF, the resultant desired signal is further digitalized by a low sampling-rate ADC. By denoting f_{ADC} as the ADC sampling rate, the output signal is given by

$$
\begin{aligned}
&r^k_{\mathrm{ADC},i}[m]\\
&\simeq \sum_{l=0}^{L-1}\left[\sqrt{P_{\mathrm{SPS}}}h_l^{\mathrm{S}} e^{\mathrm{IF}^k_{\frac{N}{2},i}(m\Delta t_s^k)} + w(m\Delta t_s^k)\right]\Big|_{\Delta t_s^k=\frac{1}{f_{\mathrm{ADC}}}}\\
&\simeq \sum_{l=0}^{L-1}\sqrt{P_{\mathrm{SPS}}}h_l^{\mathrm{S}} e^{-j2\pi\frac{\frac{2\alpha\Delta R}{\nu}+f_d^0}{f_{\mathrm{ADC}}}m} e^{-j2\pi f_d^0 T_{\mathrm{s}} i} e^{-j2\pi\frac{\phi_i^0}{f_{\mathrm{ADC}}}} + w_i^k[m].
\end{aligned}
\tag{36}
$$

Before presenting the AFDM parameter-oriented radar processing schemes, we discuss the phase-hopping issue in the IF signal (i.e., (27) and (36)) caused by spectrum wrapping. Define the IF signals of the kth and $(k+1)$th components in (27) to be effectively continuous if $\mathrm{IF}^k_{\frac{N}{2},i}(t) = \mathrm{IF}^{k+1}_{\frac{N}{2},i}(t)$, $t = kT/K$. Based on (27), the above equality holds when

$$
\frac{\Delta R_l B}{\nu} + \frac{v_l B(1 + kT/K)}{\nu} \in \mathbb{Z}. \tag{37}
$$

(37) is a stringent requirement since ΔR_l and v_l are unknown parameters that need to be estimated. Fig. 3 illustrates an example of the IF signal with $c_1 = \frac{1}{N}$ where (37) does not hold. Although the undesired IF signal within the hopping window, i.e., $t_s \in \mathcal{T}_k^{\mathrm{II}}$, can be suppressed by the LPF, phase discontinuities still arise between adjacent chirp components within each AFDM symbol. Such discontinuities (or hopping) pose significant challenges for radar parameter estimation. For example, they may cause increased sidelobes and spectral leakage when on-grid estimation methods, such as FFT-based techniques, are applied for range estimation [16]. To address this issue, we propose AFDM-parameter-oriented sensing algorithms.

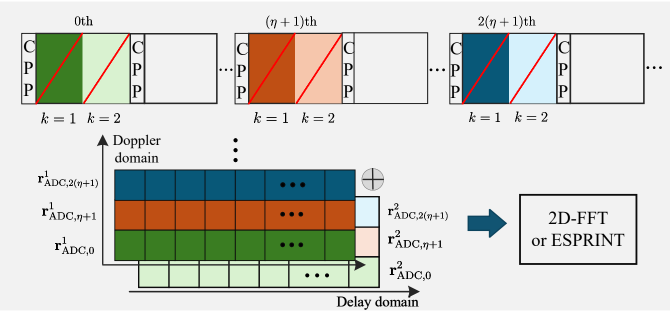

Fig. 4: Illustration of the proposed AFDM-oriented parameter estimations.

From (30), it can be observed that the Doppler term remains constant across the ISAC symbol index i and the chirp sweeping index k. This indicates Doppler and BF can be estimated based on the kth IF component across different ISAC symbols. Moreover, it is noted that the terms f_d^0 and $\mathrm{BF}^0_{\frac{N}{2},i}$ in (30) are also independent of the chirp sweeping index k. This motivates us to aggregate all K chirp components within each ISAC symbol, and then employ the aggregated signals across different ISAC symbols for joint range and velocity estimation, as illustrated in Fig. 4. Specifically, the K chirp components within the ith symbol are aggregated as follows:

$$
\mathbf{r}_{\mathrm{agg},i}[m] = \sum_{k=0}^{K-1} r^k_{\mathrm{ADC},i}[m]. \tag{38}
$$

Then, by collecting the N_s ISAC symbols into $\mathbf{R}_{\mathrm{agg}} = [\mathbf{r}^{\mathcal{T}}_{\mathrm{agg},0}, \mathbf{r}^{\mathcal{T}}_{\mathrm{agg},1}, \ldots, \mathbf{r}^{\mathcal{T}}_{\mathrm{agg},N_s-1}]$, existing algorithms such as 2D-FFT and ESPRIT can be applied to estimate f_d^0 and the beat frequency $\frac{\frac{2\alpha\Delta R_l}{\nu}+f_d^0}{f_{\mathrm{ADC}}}$ [16], [41].

D. *Performance Indicators*

We now present the performance indicators of the proposed AFDM-ISAC scheme.

1) Maximum velocity and velocity resolution: From (27), the initial phase difference of the kth chirp component between two consecutive AFDM-ISAC symbols is $\Delta\Phi \triangleq \mathrm{IF}^k_{\frac{N}{2},i+1}(0) - \mathrm{IF}^k_{\frac{N}{2},i}(0) \approx \frac{4\pi v_l T_s f_c}{\nu}$. The speed measurement is unambiguous only if $\Delta\Phi < \pi$. Hence, the maximum speed is given by

$$
v_{\max} = \frac{\nu}{4 f_c (1+\eta)(T + T_{\mathrm{CPP}})}. \tag{39}
$$

According to the Rayleigh limit, two Doppler components are resolvable when their frequency separation satisfies $\Delta f_d \geq \frac{1}{N_{\mathrm{F}}(T+T_{\mathrm{CPP}})}$, leading to the Rayleigh-limited velocity resolution as follows:

$$
v_{\mathrm{res}}^{\mathrm{Ray}} = \frac{\nu}{2N_{\mathrm{F}} f_c (T + T_{\mathrm{CPP}})}. \tag{40}
$$

It is worth noting that (40) represents a fundamental limit for classical spectral estimation methods such as the FFT-based algorithms. In practice, super-resolution algorithms, such as ESPRIT [41] adopted in this paper, can resolve targets with velocity separations well below the Rayleigh limit [42]. Specifically, the achievable velocity resolution of ESPRIT-type algorithms is governed by the estimation accuracy, i.e., the CRLB. In this paper, the CRLB-limited velocity resolution is essentially the estimation of multiple tone frequencies, which can be approximated as [43]

$$v_{\text{res}}^{\text{SR}} \approx \frac{\nu}{2\pi f_c(1+\eta)(T+T_{\text{CPP}})}\sqrt{\frac{6}{N_{\text{s}}(N_{\text{s}}^2-1)\cdot\text{SNR}}}, \tag{41}$$

where SNR refers to the received signal-to-noise ratio (SNR).

2) Maximum range and range resolution: The system's maximum range depends on the guard-band length (i.e., N_{G}^{S}), the reference delay (i.e., τ_{ref}), and the ADC sampling rate. Following the Nyquist theorem, the ADC rate must be at least twice the maximum BF. From (35), it follows that

$$R_{\max} = \min\left\{\frac{N_{\text{G}}^{\text{S}}T}{2N} + R_{\text{ref}},\quad \frac{f_{\text{ADC}}\nu}{4\alpha} + R_{\text{ref}}\right\}. \tag{42}$$

A straightforward approach for extending the maximum detection range is to increase the number of sensing guard subcarriers N_{G}^{S}, which, however, comes at the cost of reduced communication SE. In contrast, (42) reveals that by introducing a reference delay to the local chirp signal, as defined in (21), the maximum detection range can be flexibly enlarged by simply increasing τ_{ref}, without sacrificing any communication resources.

To resolve two closely spaced targets in range, the spacing between their BF tones must exceed the Rayleigh limit, i.e., $\Delta f_{\text{IF}} \geq \frac{1}{T_{\text{obs}}}$, where T_{obs} denotes the observation time of the IF signal. Since the observation time satisfies $T_{\text{obs}} \leq \frac{T}{K}$ and the BF is related to range by $f_{\text{IF}} = \frac{2\alpha R}{\nu}$, the Rayleigh-limited range resolution is given by

$$R_{\text{res}}^{\text{Ray}} = \frac{\nu}{2\alpha T_{\text{obs}}} \leq \frac{K\nu}{2\alpha T}. \tag{43}$$

Similar to the velocity case, the range resolution of super-resolution-based algorithms can be approximated as [43]

$$R_{\text{res}}^{\text{SR}} \approx \frac{\nu}{2\pi\alpha/f_{\text{ADC}}}\sqrt{\frac{6}{M_{\text{ADC}}(M_{\text{ADC}}^2-1)\cdot\text{SNR}}}, \tag{44}$$

where $M_{\text{ADC}} = \lfloor f_{\text{ADC}}T_{\text{obs}}\rfloor$ is the number of ADC samples.

3) Normalized communication efficiency: The normalized communication efficiency (NCE) is defined as

$$\begin{aligned}\eta_{\text{NCE}} &= \frac{\text{Number of communication subcarriers}}{\text{Number of total subcarriers}}\\ &= \frac{N - 2N_{\text{G}}^{\text{D}} - 2N_{\text{G}}^{\text{S}} - 3 + \eta N}{(1+\eta)N}\\ &= 1 - \frac{1}{1+\eta}\cdot\frac{2N_{\text{G}}^{\text{D}} + 2N_{\text{G}}^{\text{S}} + 3}{N}.\end{aligned} \tag{45}$$

From (45), it can be observed that the NCE is dominated by the parameter η and the number of guard subcarriers. A larger η means higher communication SE. However, increasing η comes at the cost of reducing the maximum unambiguous detectable speed $v_{\max}$, as given in (39). To illustrate this trade-off, we consider a typical parameter setting with $\Delta f = 15$ kHz, $N = 256$, and a CPP overhead ratio of 0.09. The corresponding maximum detectable speeds for $\eta = \{0, 1, 2, 3, 4\}$ are $v_{\max} = \{925, 462, 308, 231, 185\}$ km/h, respectively. It can be observed that even when $\eta = 4$, the system can still support a maximum speed of 185 km/h. This indicates that η has a large degree of freedom for flexible selection, allowing the system to achieve both high communication SE and satisfactory sensing performance requirements simultaneously.

V. THE PROPOSED CHANNEL ESTIMATION SCHEMES

Based on the proposed AFDM-ISAC frame structure, this section studies efficient channel estimation methods. We employ the BEM to characterize time-varying channels due to its simplicity and analytical tractability [9]. Specifically, we begin with a GCE-BEM–assisted estimator, followed by a power-allocation strategy and a KF-BEM channel estimation method tailored to the frame-based design.

A. The GCE-BEM

In this paper, we employ the GCE-BEM to model $h_i(n,p)$ in (14) [9], i.e.,

$$h_i\left(n,p\right) = \sum_{q=0}^{Q-1} b_n^q c_{i,p}^q, \tag{46}$$

where $b_n^q = \mathrm{e}^{\frac{j2\pi(q-Q/2)n}{NR}}$ denotes the qth basis coefficient at the nth entry, $c_{i,p}^q$ denotes the corresponding BEM coefficient at the ith symbol of the pth tap, and Q is the dimension of the basis vector that satisfies $Q \geq 2\lceil Rf_{\text{d,max}}NT_s\rceil$ with $f_{\text{d,max}}$ denoting the maximum Doppler frequency (Hz) and R representing a positive integer resolution parameter. In this paper $R = 2$ is considered as it yields sufficiently low error, and $R \geq 3$ provides negligible benefit, as shown in [9].

Let $\mathbf{b}^q = [b_0^q, b_1^q, \ldots, b_{N-1}^q]^{\mathcal{T}}$, $\mathbf{c}_i^q = [c_{i,0}^q, c_{i,1}^q, \ldots, c_{i,P-1}^q]^{\mathcal{T}}$ and $\mathbf{B}^q = \text{diag}\{\mathbf{b}^q\}$. Then, the time-domain channel can be expressed in matrix form as

$$\mathbf{H}_i = \sum_{q=0}^{Q-1}\sum_{p=0}^{P-1} c_{i,p}^q \mathbf{B}^q \mathbf{\Pi}^p \overset{\text{(i)}}{=} \sum_{q=0}^{Q-1} \mathbf{B}^q \mathbf{F}_N^{\mathcal{H}} \text{diag}\{\mathbf{F}_{N\times P}\mathbf{c}_i^q\}\mathbf{F}_N, \tag{47}$$

where $\mathbf{\Pi}$ denotes a circulant matrix, and (i) is obtained with the aid of DFT, i.e., $\sum_{p=0}^{P-1} c_{i,p}^q \mathbf{\Pi}^p = \mathbf{F}_N^{\mathcal{H}}\text{diag}\{\mathbf{F}_{N\times P}\mathbf{c}_i^q\}\mathbf{F}_N$, where $\mathbf{F}_{N\times P}$ denotes the first P columns of the DFT matrix $\mathbf{F}_N$.

Substituting (47) into (17), the received signal with BEM can be expressed as

$$\begin{aligned}\mathbf{y}_i &= \sum_{q=0}^{Q-1} \mathbf{A}\mathbf{B}^q\mathbf{F}^{\mathcal{H}}\text{diag}\{\mathbf{F}_{N\times P}\mathbf{c}_i^q\}\mathbf{F}\mathbf{A}^{\mathcal{H}}\mathbf{x}_i + \mathbf{n}_i\\ &= \sum_{q=0}^{Q-1} \mathbf{A}\mathbf{B}^q\mathbf{F}^{\mathcal{H}}\text{diag}\{\mathbf{F}\mathbf{A}^{\mathcal{H}}\mathbf{x}_i\}\mathbf{F}_{N\times P}\mathbf{c}_i^q + \mathbf{n}_i.\end{aligned} \tag{48}$$

We denote $\mathbf{x}_{i,\text{p}}$ and $\mathbf{x}_{i,\text{d}}$, $i \in \mathcal{I}_{\text{ISAC}}$ as the associated pilot and data sections of the ith symbol, respectively. Then, (48) can be rewritten as

$$\begin{aligned}\mathbf{y}_i = &\sum_{q=0}^{Q-1} \mathbf{A}\mathbf{B}^q\mathbf{F}^{\mathcal{H}}\text{diag}\{\mathbf{F}\mathbf{A}_{\text{p}}^{\mathcal{H}}\mathbf{x}_{i,\text{p}}\}\mathbf{F}_P\mathbf{c}_i^q +\\ &\sum_{q=0}^{Q-1} \mathbf{A}\mathbf{B}^q\mathbf{F}^{\mathcal{H}}\text{diag}\{\mathbf{F}\mathbf{A}_{\text{d}}^{\mathcal{H}}\mathbf{x}_{i,\text{d}}\}\mathbf{F}_P\mathbf{c}_i^q + \mathbf{n}_i\\ \equiv &\,\mathbf{M}_{i,\text{p}}\mathbf{c}_i + \mathbf{M}_{i,\text{d}}\mathbf{c}_i + \mathbf{n}_i, i \in \mathcal{I}_{\text{ISAC}},\end{aligned} \tag{49}$$

where $\mathbf{M}_{i,\mathrm{p}} = [\mathbf{M}^0_{i,\mathrm{p}}, \mathbf{M}^1_{i,\mathrm{p}}, \ldots, \mathbf{M}^{Q-1}_{i,\mathrm{p}}]$, $\mathbf{M}^q_{i,\mathrm{p}} = \mathbf{A}\mathbf{B}^q\mathbf{F}^{\mathcal{H}}\mathrm{diag}\{\mathbf{F}\mathbf{A}^{\mathcal{H}}_{\mathrm{p}}\mathbf{x}_{i,\mathrm{p}}\}\mathbf{F}_P$, $\mathbf{M}_{i,\mathrm{d}} = [\mathbf{M}^0_{i,\mathrm{d}}, \mathbf{M}^1_{i,\mathrm{d}}, \ldots, \mathbf{M}^{Q-1}_{i,\mathrm{d}}]$, $\mathbf{M}^q_{i,\mathrm{d}} = \mathbf{A}\mathbf{B}^q\mathbf{F}^{\mathcal{H}}\mathrm{diag}\{\mathbf{F}\mathbf{A}^{\mathcal{H}}_{\mathrm{d}}\mathbf{x}_{i,\mathrm{d}}\}\mathbf{F}_P$ and $\mathbf{c}_i = [\mathbf{c}_i^{0,\mathcal{T}}, \mathbf{c}_i^{2,\mathcal{T}} \ldots, \mathbf{c}_i^{Q-1}]^{\mathcal{T}}$. In the following, the matrices $\mathbf{M}_{i,\mathrm{p}}$ and $\mathbf{M}_{i,\mathrm{d}}$ are referred to as measurement matrices. In addition, denote $\mathbf{T}_{\mathrm{p}} = [\mathbf{I}_N]_{\mathcal{N}_{\mathrm{p}}}$ as the sub-matrix of $\mathbf{I}_N$ obtained by selecting the rows indexed by $\mathcal{N}_{\mathrm{p}}$, where $\mathcal{N}_{\mathrm{p}} = \{n | n \in [\frac{N}{2} - N_{\mathrm{G}}^{\mathrm{D}} - N_{\mathrm{G}}^{\mathrm{S}} - 1, \frac{N}{2} + N_{\mathrm{G}}^{\mathrm{D}} + 1]\}$ is the index set of the pilot sections. Multiplying $\mathbf{T}_{\mathrm{p}}$ on both sides of (49) leads to

$$\mathbf{y}_{i,\mathrm{p}} = \widetilde{\mathbf{M}}_{i,\mathrm{p}}\mathbf{c}_i + \underbrace{\widetilde{\mathbf{M}}_{i,\mathrm{d}}\mathbf{c}_i + \widetilde{\mathbf{n}}_i}_{\text{Interference}}, \tag{50}$$

where $\mathbf{y}_{i,\mathrm{p}} = \mathbf{T}_{\mathrm{p}}\mathbf{y}_i$ denotes the received pilot section, $\widetilde{\mathbf{M}}_{i,\mathrm{p}} = \mathbf{T}_{\mathrm{p}}\mathbf{M}_{i,\mathrm{p}}$, $\widetilde{\mathbf{M}}_{i,\mathrm{d}} = \mathbf{T}_{\mathrm{p}}\mathbf{M}_{i,\mathrm{d}}$, $\widetilde{\mathbf{n}}_i = \mathbf{T}_{\mathrm{p}}\mathbf{n}_i$ denote the transmitted pilot section, the interference from the data subcarriers and the corresponding noises term, respectively. Finally, the linear minimum mean square error (LMMSE) estimator is applied to obtain the BEM coefficients, i.e.,

$$\mathbf{W}_i^{\mathrm{LMMSE}} = \mathbf{R}_{\mathrm{c}}\widetilde{\mathbf{M}}^{\mathcal{H}}_{i,\mathrm{p}} \left(\widetilde{\mathbf{M}}_{i,\mathrm{p}}\mathbf{R}_{\mathrm{c}}\widetilde{\mathbf{M}}^{\mathcal{H}}_{i,\mathrm{p}} + \mathbf{R}_{\mathrm{d}} + \mathbf{R}_{\mathrm{n}}\right)^{-1}, \tag{51}$$

where $\mathbf{R}_{\mathrm{c}} = \mathbb{E}\{\mathbf{c}\mathbf{c}^{\mathcal{H}}\}$, $\mathbf{R}_{\mathrm{d}} = \mathbb{E}\{\widetilde{\mathbf{M}}_{i,\mathrm{d}}\mathbf{c}_i\mathbf{c}_i^{\mathcal{H}}(\widetilde{\mathbf{M}}_{i,\mathrm{d}})^{\mathcal{H}}\}\}$ and $\mathbf{R}_{\mathrm{n}} = \sigma_c\mathbf{I}_{|\mathrm{Ind_p}|}$ are the covariance matrices. The detailed derivations of $\mathbf{R}_{\mathrm{c}}$ and $\mathbf{R}_{\mathrm{d}}$ are given in Appendix A. With (51), the BEM coefficient vector is estimated by

$$\widehat{\mathbf{c}}_i = \mathbf{W}^i_{\mathrm{LMMSE}}\mathbf{y}_{i,\mathrm{p}}, i \in \mathcal{I}_{\mathrm{ISAC}}. \tag{52}$$

Finally, the estimated affine-domain channel is given by

$$\widehat{\mathbf{H}}_{\mathrm{eff},i} = \mathbf{A}\sum_{q=0}^{Q-1}\mathbf{B}^q\mathbf{F}^{\mathcal{H}}\mathrm{diag}\{\mathbf{F}_{N\times P}\widehat{\mathbf{c}}_i^q\}\mathbf{F}, i \in \mathcal{I}_{\mathrm{ISAC}}. \tag{53}$$

B. Power Allocation

Given the proposed frame structure and channel estimation scheme, it is important to investigate the power allocation between pilot and data symbols under a constrained total power budget, as defined in (9). Denote the channel estimation error matrix in the DAFT domain by $\widehat{\mathbf{H}}_{\mathrm{err},i} = \mathbf{H}_{\mathrm{eff},i} - \widehat{\mathbf{H}}_{\mathrm{eff},i}$. Using MMSE detector, the estimated symbol vector is given as

$$\widehat{\mathbf{x}}_i = \mathbf{G}^i_{\mathrm{LMMSE}}\mathbf{y}_i = \mathbf{R}_{\mathbf{x}_i}\widehat{\mathbf{H}}^{\mathcal{H}}_{\mathrm{eff},i}\left(\widehat{\mathbf{H}}_{\mathrm{eff},i}\mathbf{R}_{\mathbf{x}_i}\widehat{\mathbf{H}}^{\mathcal{H}}_{\mathrm{eff},i} + \mathbf{R}_{\mathrm{I}}\right)^{-1}\mathbf{y}_i. \tag{54}$$

To derive the SINR on the nth chirp subcarrier, we rewrite the received signal as

$$\mathbf{y}_i = \widehat{\mathbf{H}}_{\mathrm{eff},i}\mathbf{x}_i + \underbrace{\widehat{\mathbf{H}}_{\mathrm{err},i}\mathbf{x}_i + \mathbf{n}_i}_{\text{Interference+ noise}}. \tag{55}$$

Then (54) can be further written as

$$\begin{aligned}\widehat{\mathbf{x}}[n] =& \mathbf{T}_{\mathrm{est},i}[n,n]\mathbf{x}[n] \\ &+ \sum_{m\neq n}\mathbf{T}_{\mathrm{est},i}[n,m]\mathbf{x}[m] + \mathbf{T}_{\mathrm{err},i}[n,n] + \mathbf{T}_{\mathrm{n},i}[n,n],\end{aligned} \tag{56}$$

where $\mathbf{T}_{\mathrm{est},i} = \mathbf{G}^i_{\mathrm{LMMSE}}\widehat{\mathbf{H}}_{\mathrm{est},i}$, $\mathbf{T}_{\mathrm{err},i} = \mathbf{G}^i_{\mathrm{LMMSE}}\widehat{\mathbf{H}}_{\mathrm{err},i}$, $\mathbf{T}_{\mathrm{n},i} = \mathbf{G}^i_{\mathrm{LMMSE}}\widetilde{\mathbf{n}}_i$. Assuming the transmitted data has the unit power, the SINR on the nth subcarrier can be expressed as

$$\mathrm{SINR}_n = \frac{\mathbf{T}^2_{\mathrm{est},i}[n,n]}{\mathrm{Var}\left\{\sum_{m\neq n}\mathbf{T}_{\mathrm{est},i}[n,m]\mathbf{x}[m] + \mathbf{T}_{\mathrm{err},i}[n,n] + \mathbf{T}_{\mathrm{n},i}[n,n]\right\}}. \tag{57}$$

By using the central limit theorem and based on the results reported in [44, (15)-(16)], the equality in (57) can be approximated as $\mathrm{SINR}_n \approx \frac{\mathbf{T}_{\mathrm{est},i}[n,n]}{1-\mathbf{T}_{\mathrm{est},i}[n,n]}$. Note that the power of the SPS is determined by radar sensing requirements; thus, only P_{SP} needs to be optimized. Hence, the power allocation problem is formulated as

$$\begin{aligned}\max_{P_{\mathrm{PS}}} \quad & \mathrm{SINR}_n, n \in \mathcal{N}_{\mathrm{D}} \\ \text{s.t.} \quad & P_{\mathrm{SPS}} + 2P_{\mathrm{SP}} + |\mathcal{N}_{\mathrm{D}}| = P_{\mathrm{total}},\end{aligned} \tag{58}$$

where each data symbol is assumed to have unit average power, and P_{total} denotes the total available power. Once SINR_n for each data subcarrier is obtained, the average bit error rate (BER) performance can be derived by following the approach in [44, (16)–(21)]. With the statistical channel information, (58) can be resolved via Monte Carlo simulation.

C. KF-BEM Enhanced Channel Estimation

Note that once the estimated channel is obtained for the ISAC symbol based on (52) and (53), the effective channel for the subsequent pure data symbols can be predicted using (15), i.e., $\mathbf{h}_{i+1} = \widetilde{\mathbf{S}}\mathbf{h}_i$. While the state transition matrix $\widetilde{\mathbf{S}}$ enables channel prediction, $\mathbf{h}_i$ is only available through noisy observations with random dynamics, making the prediction inaccurate and prone to error propagation. Hence, we propose a KF-BEM scheme to optimally fuse both predictions and observations, thereby achieving robust channel predication under the proposed frame-based structure. The proposed KF-BEM scheme mainly consists of 1) State space model of BEM coefficients; 2) State prediction; and 3) Sate updating.

1) State space model of BEM coefficients: Using $\mathbf{h}_i = (\mathbf{I}_P \odot \mathbf{B})\mathbf{c}_i$ and (15), the state space of BEM coefficients can be expressed as

$$\begin{aligned}\mathbf{c}_{i+1} &= \mathbf{S}\mathbf{c}_i + \mathbf{v}_i, \\ \mathbf{y}_i &= \mathbf{M}_i\mathbf{c}_i + \mathbf{n}_i,\end{aligned} \tag{59}$$

where $\mathbf{S} = \left((\mathbf{I}_P \odot \mathbf{B})^{\mathcal{H}}(\mathbf{I}_P \odot \mathbf{B})\right)^{-1}(\mathbf{I}_P \odot \mathbf{B})\widetilde{\mathbf{S}}(\mathbf{I}_P \odot \mathbf{B})$ and $\mathbf{v}_i = \left((\mathbf{I}_P \odot \mathbf{B})^{\mathcal{H}}(\mathbf{I}_P \odot \mathbf{B})\right)^{-1}(\mathbf{I}_P \odot \mathbf{B})\mathbf{n}_i$. $\mathbf{M}_i$ is the measurement matrix of the transmitted data, i.e, $\mathbf{M}_i = [\mathbf{M}^0_i, \mathbf{M}^1_i, \ldots, \mathbf{M}^Q_i]$ and $\mathbf{M}^q_i = \mathbf{S}\mathbf{B}^q\mathbf{F}^{\mathcal{H}}\mathrm{diag}\{\mathbf{F}\mathbf{A}^{\mathcal{H}}\mathbf{x}_i\}\mathbf{F}_P$.

2) State prediction: In the state prediction process, *a priori* estimates of the state variable at the $(i+1)$th moment are obtained based on the *a posterior* estimates and the state transfer function. The state prediction of the state space model in (59) can be obtained as

$$\mathbf{c}_{i|i-1} = \mathbf{S}\mathbf{c}_{i-1}, \tag{60}$$

$$\mathbf{P}_{i|i-1} = \mathbf{S}\mathbf{P}_{i-1}\mathbf{S}^{\mathcal{H}} + \mathbf{V}, \tag{61}$$

where $\mathbf{P}_{i|i-1}$ and $\mathbf{P}_{i-1}$ denote the *a priori* and *a posterior* covariance matrices of the ith state variable, and $\mathbf{V} = \mathbb{E}[\mathbf{v}_i\mathbf{v}_i^{\mathcal{H}}] = \sigma_n^2\mathbf{I}_{PQ}$ denotes the covariance matrix of $\mathbf{v}_i$. Note that for the data symbols, the measurement matrix $\mathbf{M}_i$ is unknown and contains the transmitted data symbols. Hence, we propose a refined channel estimation scheme to construct the $\mathbf{M}_i$. Specifically, based on (60), *a priori* estimate of BEM coefficients $\mathbf{c}_{i|i-1}$ is first obtained, and then the estimated channel, denoted as $\widehat{\mathbf{H}}_{\mathrm{eff},i|i-1}$, can be obtained based on (53).

Algorithm 1 The Proposed KF-BEM for Frame-based Channel Estimation.

```
Initialize KF-BEM.
Step 1: If $\mod(i, \eta+1) = 0$, the BEM coefficients and channel matrix are estimated by the ISAC symbol based on (52) and (53), respectively. When the next ISAC symbol arrived, Step 2 to Step 4 are executed.
Step 2: State Prediction and Measurement Matrix Construction: The a priori estimates of the state variable $\mathbf{c}_{i|i-1}$ is calculated through (60). Then, the measurement matrix $\widehat{\mathbf{M}}_i$ can be constructed based on the resultant $\widehat{\mathbf{x}}_i$ in (62).
Step 3: State Updating: The a posterior state BEM coefficients are updated by (63). Then, the effective channel of the $i$th symbol is obtained by (53) based on the $\mathbf{c}_i$ in (63).
Step 4: Set $i = i + 1$. If $\mod(i, \eta+1) \neq 0$, repeat Step 2 and Step 3, otherwise jump back to Step 1.
```

Therefore, the ith transmitted AFDM symbol can be obtained by LMMSE equalization as

$$\widehat{\mathbf{x}}_i = \left(\widehat{\mathbf{H}}_{\text{eff},i|i-1}\widehat{\mathbf{H}}_{\text{eff},i|i-1} + \sigma_c \mathbf{I}_N\right)^{-1} \widehat{\mathbf{H}}^{\mathcal{H}}_{\text{eff},i|i-1}\mathbf{y}_i, \tag{62}$$

where $\widehat{\mathbf{x}}_i$ denotes the predicted transmitted symbols. As the transmitted symbols are chosen from the constellation alphat set $\boldsymbol{\mathcal{X}} = \{\mathcal{X}_1, \mathcal{X}_2, \ldots, \mathcal{X}_M\}$, the output of the refined channel estimation is a modulation symbol in $\boldsymbol{\mathcal{X}}$ which is the nearest one for $\widehat{\mathbf{x}}_i[n]$., i.e., $\widehat{\mathbf{x}}_i[n] = \min\limits_{\mathcal{X}_m \in \boldsymbol{\mathcal{X}}} \|\mathcal{X}_m - \widehat{\mathbf{x}}_i[n]\|^2$. Finally, the measurement matrix $\widehat{\mathbf{M}}_i$ can be constructed from $\widehat{\mathbf{x}}_i$ and will be used for state updating.

3) State updating: After the state predication, the *a posterior* state BEM coefficients are estimated through the state updating principles of Kalman filter as follows:

$$\begin{aligned} \mathbf{K}_i &= \mathbf{P}_{i|i-1}\widehat{\mathbf{M}}_i^{\mathcal{H}}\left(\widehat{\mathbf{M}}_i\mathbf{P}_{i|i-1}\widehat{\mathbf{M}}_i^{\mathcal{H}} + \mathbf{V}\right)^{-1}, \\ \mathbf{c}_i &= \mathbf{c}_{i|i-1} + \mathbf{K}_i\left(\mathbf{y}_i - \widehat{\mathbf{M}}_i\mathbf{c}_{i|i-1}\right), \\ \mathbf{P}_i &= \mathbf{P}_{i|i-1} - \mathbf{K}_i\widehat{\mathbf{M}}_i\mathbf{P}_{i|i-1}, \end{aligned} \tag{63}$$

where $\mathbf{K}_i$ denotes the Kalman gain. Based on the state prediction and updating of the Kalman filter, the *a posterior* BEM coefficient $\mathbf{c}_i$ is obtained as the output, and the effective channel $\widehat{\mathbf{H}}_{\text{eff},i}$ is obtained based on (53). Finally, the detailed steps of the proposed KF-BEM are summarized in **Algorithm 1**.

D. Benchmarking Schemes and Complexity Analysis

In this paper, the existing embedded channel estimation (ECE) scheme from [37], referred to as diagonally reconstructed ECE (DR-ECE), is employed as a benchmark. Since the original DR-ECE in [37] utilizes only a single pilot for channel estimation, we modify it here to accommodate the proposed AFDM-ISAC structure. In the modified DR-ECE scheme, the threshold-based magnitude detection on the multiple received pilots is first conducted, i.e.,

$$\widehat{\mathbf{h}}^{(m)}_{\text{eff},i}[n] = \begin{cases} \mathbf{y}^{(m)}_{\text{p},i}[n]/x^{(m)}_{\text{pilot}}, & \sum_{m=1}^{3} |\mathbf{y}^{(m)}_{\text{p},i}[n]| > \gamma_{\text{th}}, \\ 0, & \text{otherwise}, \end{cases} \tag{64}$$

where $\widehat{\mathbf{h}}^{(m)}_{\text{eff},i} \in \mathbb{C}^{(QP+1)\times 1}$ and $\mathbf{y}^{(m)}_{\text{p},i} \in \mathbb{C}^{(QP+1)\times 1}$ denote the effective channel and received data associated with the pth pilot, respectively [37]. The DR-ECE scheme rely on the integer delay to reconstruct the channel. For multiple pilots, the integer delay is estimated based on the combined channel vector $\sum_{m=1}^{3} |\widehat{\mathbf{h}}^{(m)}_{\text{eff},i}[n]|$. Then, the channel is reconstructed for each pilot using [(41), [37]]. Denote the $\widehat{\mathbf{H}}^{(m)}_{\text{eff},i}$ by the reconstructed channel based on the mth pilot, the final reconstructed channel is given by $\widehat{\mathbf{H}}_{\text{est},i} = \frac{1}{3}\sum_{m=1}^{3} \widehat{\mathbf{H}}^{(m)}_{\text{eff},i}$.

TABLE I: Simulation Parameters

System Parameters	**Values**
Center frequency	4 GHz
Num. of subcarriers	256
CPP length	24
Subcarrier spacing	$\Delta f = 15$ kHz
Frame length	64 symbols
AFDM parameters	$c_2 = c_1 = \frac{K}{2N}$, $K \in \{1, 2, \ldots, 5\}$.
Sensing Parameters	**Values**
Sensing guard length	$N_{\text{G}}^{\text{S}} = 28$
Num. of Targets	$L = 2$
Number. of data symbols	$\boldsymbol{\eta} = [0, 1, 2, 3, 4]$
Target speed	$\mathcal{U}[v_{\text{min}}, v_{\text{max}}], v_{\text{max}} = \{925, 462, 308, 231, 185\}$ km/h corresponds to $\boldsymbol{\eta}$, and $v_{\text{min}} = 10$.
Target range	$\mathcal{U}[R_{\text{min}}, R_{\text{max}}] = \mathcal{U}[200, 500]$ m
LPF	Butterworth LPF of 20 order
ADC sampling rate	$f_{\text{IF}} = 4\frac{\alpha R_{\text{max}}}{\nu}$.
Sensing channel model	LoS with pass loss factor of 2
Parameter estimation	ESPRINT [41]
Communication Parameters	**Values**
User speed	$v_{\text{ue}} \in \{160, 600\}$ km/h
Number of path	$P \in \{4, 8\}$
BEM parameters	$R = 2, Q = 4$
Pilot length	$N_{\text{G}}^{\text{D}} = (Q+1)(l_{\text{max}}+1)$
Doppler model	Jakes' model

For the proposed BEM-assisted channel estimation for ISAC symbols, the computation of $\mathbf{R}_{\text{I}}$ and $\mathbf{R}_{\text{c}}$ can be pre-calculated based on the maximum Doppler frequency and the number of paths. Thus, the complexity is mainly dominated by the matrix inversion in (51). Moreover, since the BEM approach reduces the number of estimated parameters from N^2 to QP compared to traditional MMSE-based methods, the complexity of the proposed scheme can be approximated as $\mathcal{O}(|\mathcal{N}_{\text{P}}|^2)$. For the modified DR-ECE, complexity is primarily determined by (64) and the channel reconstruction step, approximated as $\mathcal{O}(3PN + Q)$. Finally, the proposed KF-BEM method introduces an additional complexity of approximately $\mathcal{O}(N^2)$ due to the refined channel estimation in (62).

VI. NUMERICAL RESULTS

In this section, we evaluate the sensing and communication performance of the proposed AFDM-ISAC systems. The detailed simulation parameters are summarized in Table I. The parameters $N_{\text{G}}^{\text{S}} = 28$, the ADC sampling rate, and the LPF parameters are chosen to satisfy the maximum detection range requirement R_{max}, as specified in (42). The proposed scheme is applicable to multiple target detection, as each target produces a distinct IF component that can be resolved provided the targets are separated in range or velocity. Without loss of

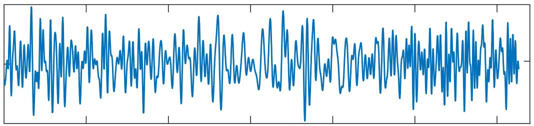

(a) Mixed signal before LPF

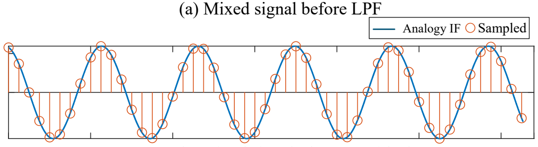

(b) Mixed signal after LPF (ideal)

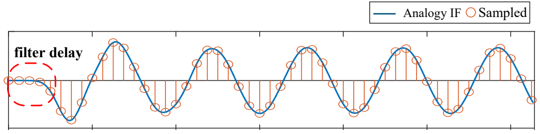

(c) Mixed signal after LPF (Guard = 28)

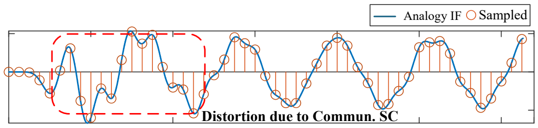

(d) Mixed signal after LPF (Guard = 24)

Fig. 5: The dechirped signal after and before the LPF.

generality, $L = 2$ sensing targets are considered for illustration purposes.

Conventional schemes require a wideband ADC operating at the full system bandwidth $f_{\text{ADC}} \geq B = N\Delta f$. In contrast, the proposed scheme only requires $f_{\text{ADC}} \geq 4\alpha\Delta R_{\max}/\nu$. With the parameters in Table I ($c_1 = \frac{3}{2N}$, $\Delta R_{\max} = 300$ m), this yields $f_{\text{ADC,min}} \approx 826.3$ kHz, which is approximately $4.6\times$ lower than $B = 3.84$ MHz. Also, full-duplex SIC is well recognized as one of the most challenging and costly components in monostatic ISAC systems. The proposed analog-domain sensing receiver completely eliminates this requirement through the LPF-based leakage suppression.

Fig. 5 presents an example of the original mixed signal, along with its counterparts after passing through the LPF and ADC. As seen from 5(b), the proposed LPF can well eliminate the interference from the communication subcarriers. As mentioned above, the sampling frequency required by the ADC is much smaller than that of the system bandwidth.

A. Sensing Performance Comparison

To evaluate the sensing performance, we consider two targets whose distances are randomly drawn from a uniform distribution $\mathcal{U}[R_{\min}, R_{\max}]$. We assume an LoS channel between the sensing targets and the ISAC platform. Accordingly, the average received SNR is modeled as

$$[\text{SNR}]_{\text{dB}} = 10\log_{10}\left(\frac{1}{L}\sum\nolimits_{l=0}^{L-1} P_{\text{SPS}} R_l^{-\alpha_{\text{LoS}}} \varsigma_{\text{RCS}}\right)/\sigma_s, \quad (65)$$

where ς_{RCS} denotes the RCS attenuation factor. The existing OFDM-, OTFS-, and AFDM-based ISAC schemes are considered as benchmark sensing schemes [25], [45]. For a fair comparison, the number of subcarriers employed for OFDM-ISAC sensing is set to be equal to the number of guard subcarriers in the proposed AFDM-ISAC scheme. For both the conventional OTFS- and AFDM-based ISAC schemes, a dedicated sensing subcarrier with guard length N_{G}^{S} is employed. Sensing is conducted based on the received pilot sections in the frequency, delay-Doppler, and affine domains for the OFDM-, OTFS-, and AFDM-based ISAC schemes, respectively. All waveforms in the simulations are generated using a raised-cosine filter with a roll-off factor of 0.1 to obtain continuous-time waveforms.

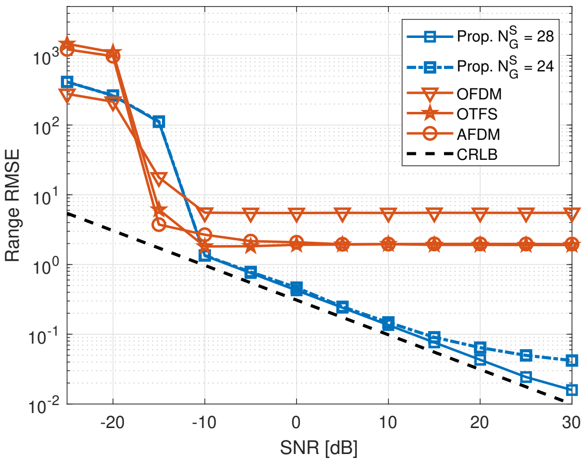

(a) Range RMSE.

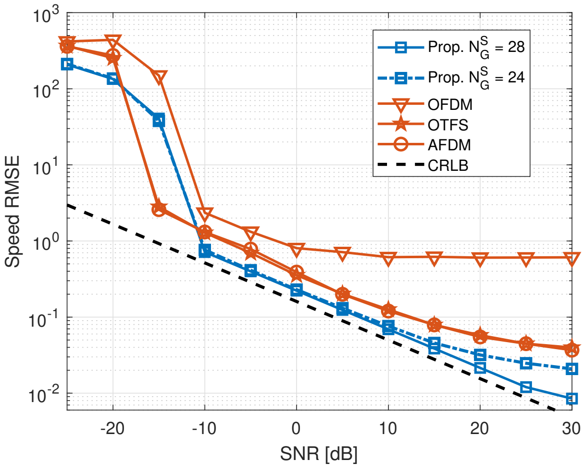

(b) Speed RMSE.

Fig. 6: Range and speed RMSE of the proposed AFDM-ISAC ($c_1 = \frac{2}{2N}$).

Fig. 6 illustrates the RMSE performance of range and speed estimations with $c_1 = \frac{2}{2N}$, based on the simulation parameters provided in TableI. For the benchmark AFDM scheme, the same c_1 is adopted. From Fig. 6, it is observed that the proposed scheme achieves the best RMSE performance for SNR > 10 dB. For the proposed scheme with $N||\text{G}^{\text{S}} = 24$, an error floor is observed, primarily due to interference from communication subcarriers caused by Doppler spread. This effect is also evident in the IF signal shown in Fig. 5. In contrast, OFDM-, OTFS-, and AFDM-based benchmarks exhibit prominent error floors in RMSE, primarily caused by waveform distortion introduced during practical digital implementations, which may not be mitigated by simply increasing the SNR. The proposed AFDM-ISAC scheme operates in the analog domain and the waveform

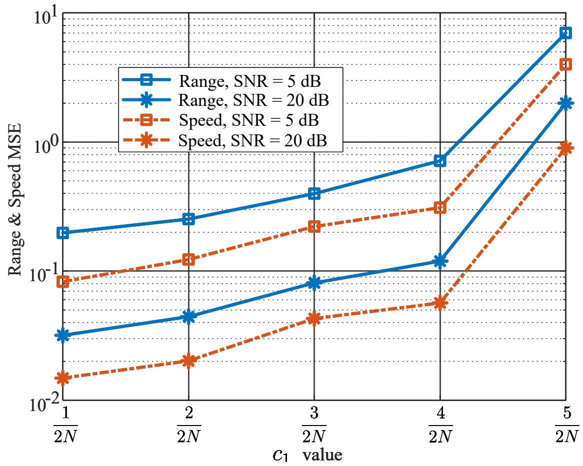

Fig. 7: Range and speed RMSE for different c_1 values.

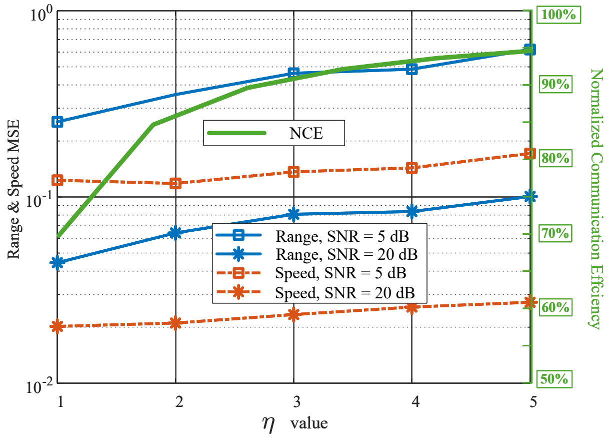

Fig. 8: Trade-off between sensing performance and communication NSE via η.

distortion caused by pulse shaping manifests predominantly as high-frequency components in the IF signal. These high-frequency distortion components can be effectively suppressed by the LPF prior to ADC sampling. Consequently, with a sufficiently large guard interval, the RMSE performance of the proposed AFDM-ISAC approaches the CRLB. Similar trends are observed for velocity estimation RMSE.

Fig. 7 further evaluates the range and speed RMSE for different values of c_1. It can be observed that both the range and speed RMSE increase with larger values of c_1. This degradation is primarily due to the reduced observation duration of the IF for larger c_1, due to the increased propagation delay of the echoes from the sensing targets. From the perspective of sensing performance and pilot overhead, a smaller value of c_1 is preferred. In the next section, we will demonstrate that moderate c_1 values, which yield favorable sensing performance, can also achieve a desirable trade-off between sensing accuracy and communication performance.

Fig. 8 shows the trade-off between sensing performance and NCE, i.e., $\eta_{\rm NCE}$ defined in (45), for different values of η. It is observed that both the range and speed RMSE degrade as η increases. This is expected, as η directly controls both the number of ISAC symbols and the number of communication subcarriers. The proposed AFDM-ISAC scheme features a flexible frame structure that enables NCE enhancement by appropriately tuning η. Since ISAC symbols also carry data subcarriers, the scheme maintains favorable NCE performance even when $\eta = 0$, i.e., when all symbols are configured as ISAC symbols. More importantly, increasing η leads to only a slight degradation in speed RMSE while achieving a significant gain in NCE. This trade-off is reasonable because increasing η effectively downsamples the IF signal in the Doppler domain. Provided that the maximum target speed satisfies $v_l \leq v_{\max}$, the speed RMSE remains within acceptable bounds.

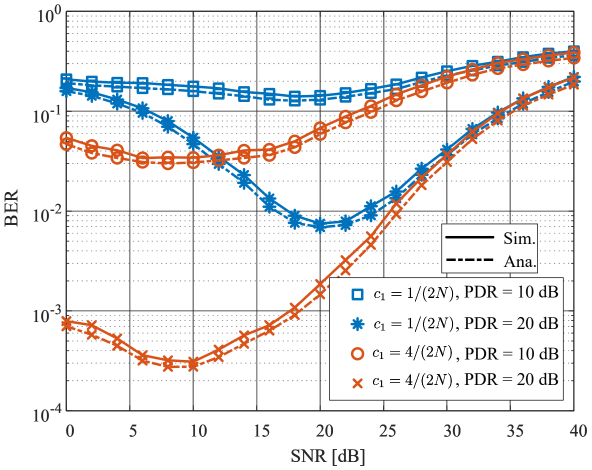

Fig. 9: Simulated and analytic BER performance for different power allocation factors.

B. *Communication Performance*

In this section, we evaluate the communication performance of the proposed AFDM-ISAC system. The detailed simulation parameters are summarized in Table I. For simplicity, we set $Q = 4$ for both low- and high-mobility user scenarios. Unless otherwise stated, $\eta = 0$ is assumed in Figs. 9–11.

Fig. 9 presents both the simulated and analytical BER performance under varying pilot-to-data ratio (PDR), defined as $\mathrm{PDR} = 10\log\frac{P_{\rm sp}}{P_{\rm d}}$ [dB], at a user mobility of 600 km/h. As observed, the BER initially improves with increasing SNR, owing to more accurate channel estimation. However, beyond the optimal point, the BER begins to degrade as less power is allocated to the data symbols. Furthermore, when the modulation parameter c_1 takes a larger value (e.g., $c_1 = \frac{4}{2N}$), the optimal BER can be achieved with relatively lower pilot power, indicating more efficient power utilization.

Fig. 10 compares the BER performance of the proposed BEM-assisted scheme with the EPA-RC channel estimation method under user mobilities of 160 km/h and 600 km/h. In this comparison, "EPA-RC, Th" refers to a threshold-based method is used to estimate the path locations, as described in (64), while "EPA-RC, LB" represents a performance lower bound, assuming perfect knowledge of the path locations at the receiver. The key observations from the results are summarized as follows:

- The gap between the "EPA-RC, LB" and "EPA-RC, Th" schemes is small, indicating that the threshold in this paper is well designed. While EPA-RC slightly outperforms

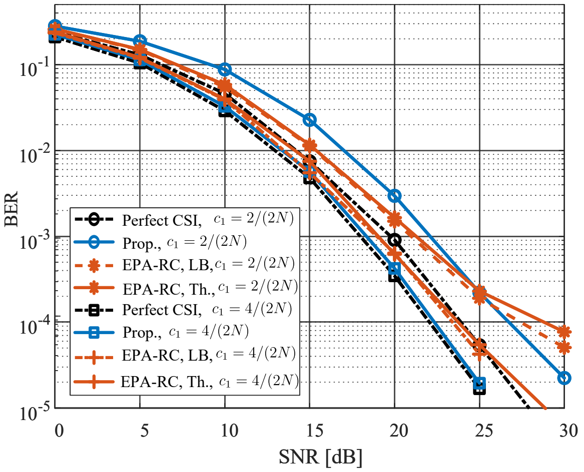

(a) 160 km/h.

Figures/BER_600.pdf

(b) 600 km/h.

Fig. 10: BER comparisons of different channel estimation schemes.

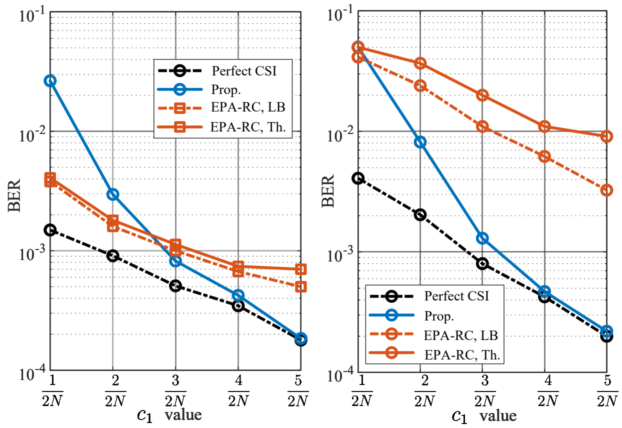

(a) 160 km/h

(b) 600 km/h

Fig. 11: BER v.s c_1 values at SNR= 20 dB.

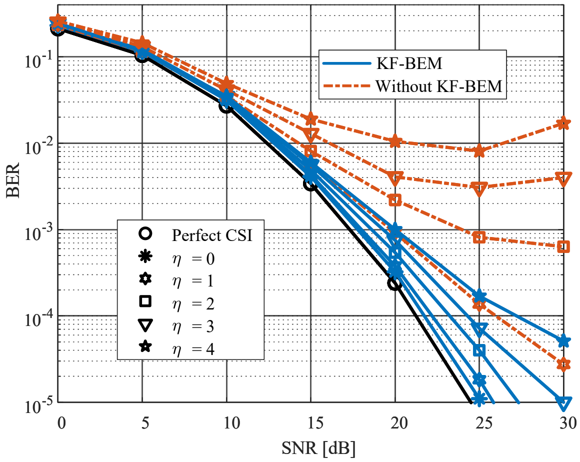

Fig. 12: BER performance of the proposed KF-BEM for different η.

the proposed BEM-assisted channel estimation method for $c_1 = \frac{2}{2N}$ at 160 km/h in the low SNR regime, the proposed scheme demonstrates a clear advantage at higher mobility. In particular, under a user mobility of 600 km/h, the proposed approach significantly outperforms the EPA-RC method across the entire SNR range.

- An SNR gap between $c_1 = \frac{2}{2N}$ and $c_1 = \frac{4}{2N}$ is observed under the perfect channel state information (CSI) case. This is expected, as more power is allocated to pilot symbols in the $c_1 = \frac{2}{2N}$ setting, which reduces the effective SNR available for data symbols and consequently degrades BER performance.
- Our proposed BEM-assisted channel estimation approach achieves robust BER performance even at a user mobility of 600 km/h. Notably, when $c_1 = \frac{4}{2N}$, the proposed scheme closely approaches the performance of the perfect CSI benchmark, highlighting its effectiveness in high-mobility scenarios.

Fig. 11 further illustrates the BER performance across different values of c_1 at SNR $= 20$ dB. One can see that the proposed BEM-assisted channel estimation progressively approaches the performance of the perfect CSI case as c_1 increases. In particular, the performance gap becomes negligible for $c_1 \geq \frac{4}{2N}$. Additionally, the BER under perfect CSI also improves with increasing c_1. The reasons are two-fold: 1) larger c_1 values require less pilot power for reliable channel estimation, allowing more transmit power to be allocated to data symbols; and 2) the AFDM waveform inherently offers better BER performance at higher c_1, even when the data symbol power is fixed. Furthermore, while the EPA-RC channel estimation slightly outperforms the proposed scheme for $c_1 = \frac{1}{2N}$ and $\frac{2}{2N}$ at a user mobility of 160 km/h, its performance degrades significantly in high-mobility scenarios (e.g., 600 km/h). Based on Fig. 7, $c_1 \in \left\{\frac{2}{2N}, \frac{3}{2N}, \frac{4}{2N}\right\}$ yields a desirable trade-off between sensing accuracy and communication performance under the considered system configurations.

Fig. 12 shows the BER performance of the proposed KF-BEM channel estimation scheme, where $c_1 = \frac{4}{2N}$ and a

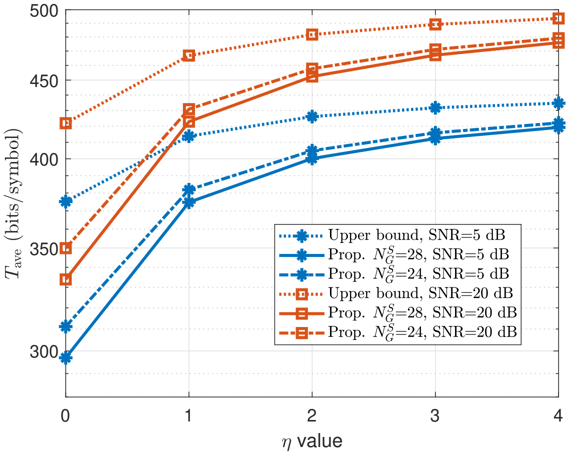

Fig. 13: Average throughput ($T_{\rm ave}$) comparison for different η and $N_{\rm G}^{\rm S}$ values.

user speed of 600 km/h are considered. As can be seen from the figure, the proposed KF-BEM scheme maintains favorable BER performance for $0 \leq \eta \leq 3$. However, for $\eta = 4$, a noticeable performance degradation appears at high SNRs due to increased channel variation. More importantly, in the absence of KF-BEM tracking, the BER performance degrades significantly as η increases, and an error floor is observed at high SNRs, primarily due to error propagation caused by inaccurate channel estimation. These results show the theoretical advantage of the proposed KF-BEM: since the Kalman filter recursively fuses the predicted state from (60) with the current observation via (63), it yields a lower or equal MSE estimation compared to the one-shot LMMSE estimator in (51). This gain becomes more pronounced as η increases, since pure data symbols lack dedicated pilots and must rely entirely on temporal prediction and tracking.

Finally, Fig. 13 compares the achieved average throughput of the proposed AFDM-ISAC frame structure with the KF-BEM, which is defined as

$$T_{\rm ave} = \log_2(M)(1 - {\rm BER}) \underbrace{\frac{N - 2N_{\rm G}^{\rm D} - 2N_{\rm G}^{\rm S} - 3 + \eta N}{1 + \eta}}_{\text{Num. of Commun. Subcarriers}}. \tag{66}$$

The curves labelled “upper bound” in Fig. 13 correspond to the case where all subcarriers are allocated for communication, i.e., $N_{\rm G}^{\rm S} = 0$. It can be observed from Fig. 13 that a throughput loss of approximately 50 bits/symbol is incurred when $\eta = 0$, which corresponds to the configuration that achieves the best sensing performance, as shown in Fig. 8. However, as η increases, the throughput of the proposed scheme progressively approaches the upper bound, provided that the maximum target speed remains within the unambiguous range defined in (39). This further shows the trade-off of the proposed AFDM-ISAC frame structure in between sensing accuracy and communication throughput through the tuning of η and $N_{\rm G}^{\rm S}$.

VII. CONCLUSION

In this paper, we proposed a practical and flexible AFDM-ISAC framework. A novel frame structure consists of ISAC symbol and pure data symbol was first designed, upon which each ISAC symbol embeds a single chirp subcarrier for both sensing and channel estimation. This enables full-bandwidth sensing with minimum sacrificing of communication rate. To overcome hardware limitations and reduce system complexity, an analog-domain sensing receiver equipped with a carefully designed LPF was also introduced. Our proposed design not only suppresses interference from communication subcarriers but also mitigates ADC saturation, thus eliminating the need for costly full-duplex circuits. Furthermore, an AFDM parameters-guided sensing aggregation algorithm was proposed in the digital domain to enhance sensing robustness. On the communication side, we proposed a GCE-BEM-assisted low complexity channel estimation scheme. Power allocation between pilot and data symbols was optimized, and a GCE-BEM-based Kalman filter was developed for reliable frame-based channel estimation. Extensive simulation results validated the proposed AFDM-ISAC design, demonstrating superior performance over existing OFDM, OTFS, and AFDM baselines in terms of sensing accuracy, communication reliability, hardware simplicity, and system flexibility. In particular, it was found that $c_1 \in \{\frac{2}{2N}, \frac{3}{2N}, \frac{4}{2N}\}$ and choosing the pure-data-to-ISAC symbol ratio $\eta \in \{1, 2, 3\}$ can achieve favorable performance in both sensing and communication.

Future work includes extending the proposed framework to multi-antenna systems for three-dimensional radar estimation (e.g., angle of arrival/departure), generalizing to bistatic and multistatic configurations, investigating nonlinear impairments such as Doppler scaling errors and hardware nonlinearities, and validating the proposed design through hardware prototyping.

APPENDIX A
DERIVATION OF $\mathbf{R}_{\rm C}$ AND $\mathbf{R}_{\rm D}$

1) Derivation of $\mathbf{R}_c$*:* Let us rewrite (46) in the vector form as $\mathbf{h}_{i,p} = \mathbf{B}\mathbf{c}_{i,p}$, where $\mathbf{B} = [\mathbf{b}_0, \mathbf{b}_1, \ldots, \mathbf{b}_{N-1}]^{\mathcal{T}}$. Then, one has $\mathbf{c}_{i,p} = \left(\mathbf{B}^{\mathcal{H}}\mathbf{B}\right)^{-1}\mathbf{B}^{\mathcal{H}}\mathbf{h}_{i,p}$. Accordingly, the corelation matrix of the BEM coefficient at the pth can be expressed as

$$\mathbf{R}_{{\rm c},i,p} = \mathbb{E}\{\mathbf{c}_{i,p}\mathbf{c}_{i,p}^{\mathcal{H}}\} = \Big(\mathbf{B}^{\mathcal{H}}\mathbf{B}\Big)^{-1}\mathbf{B}^{\mathcal{H}}\mathbf{R}_{{\rm h},i,p}\mathbf{B}\Big(\mathbf{B}^{\mathcal{H}}\mathbf{B}\Big)^{-1}, \tag{67}$$

where $\mathbf{R}_{{\rm h},i,p} = \mathbb{E}\{\mathbf{h}_{i,p}\mathbf{h}_{i,p}^{\mathcal{H}}\}$. In this paper, we consider channel taps as complex Gaussian processes of variances of zero mean and with wide sense $\sigma_{{\rm h},p}$, which follow the Jakes power spectrum of the maximum Doppler frequency $f_{\rm d,\,max}$, then

$$\begin{aligned} [\mathbf{R}_{{\rm h},i,p}]_{n,m} &= \mathbb{E}\{h_i(m,p)h_i^*(m,l)\} \\ &= \sigma_{{\rm h},p} J_0\left(2\pi f_{\rm d,max}(m-n)T_{\rm s}\right), \end{aligned} \tag{68}$$

where $J_0(\cdot)$ is the Bessel function of first kind and order zero.

2) Derivation of $\mathbf{R}_d$*:* Denote $\mathbf{D}_1 = [\mathbf{A}\mathbf{B}^0\mathbf{F}^{\mathcal{H}}, \mathbf{A}\mathbf{B}^1\mathbf{F}^{\mathcal{H}}, \ldots, \mathbf{A}\mathbf{B}^{Q-1}\mathbf{F}^{\mathcal{H}}]$, $\mathbf{D}_2 = \mathbf{I}_Q \otimes {\rm diag}\{\mathbf{F}\mathbf{A}_{\rm d}^{\mathcal{H}}\mathbf{x}_{i,{\rm d}}\}\mathbf{F}_P$. Then, one has

$$\begin{aligned} \mathbf{R}_{\rm d} &= \mathbb{E}\{\widetilde{\mathbf{M}}_{i,{\rm d}}\mathbf{c}_i\mathbf{c}_i^{\mathcal{H}}(\widetilde{\mathbf{M}}_{i,{\rm d}})^{\mathcal{H}}\} = \mathbf{D}_1\mathbb{E}\{\mathbf{D}_2\mathbf{c}\mathbf{c}^{\mathcal{H}}\mathbf{D}_2^{\mathcal{H}}\}\mathbf{D}_1^{\mathcal{H}} \\ &= \mathbf{D}_1\mathbb{E}\{\mathbf{I}_{Q+1} \otimes {\rm diag}\{\mathbf{F}\mathbf{A}^{\mathcal{H}}\mathbf{x}_{i,{\rm d}}\}\mathbf{I}_Q \otimes \mathbf{F}_L\mathbf{c}_i\mathbf{c}_i^{\mathcal{H}} \\ &\quad (\mathbf{I}_Q \otimes \mathbf{F}_P)^{\mathcal{H}}(\mathbf{I}_Q \otimes {\rm diag}\{\mathbf{F}\mathbf{A}^{\mathcal{H}}\mathbf{x}_{i,{\rm d}}\})^{\mathcal{H}}\}\mathbf{D}_1^{\mathcal{H}} \\ &= \mathbf{D}_1(\mathbf{I}_Q \otimes \mathbf{F}\mathbf{A}_{\rm d}^{\mathcal{H}}\sigma_{\rm d}\mathbf{A}_{\rm d}\mathbf{F}^{\mathcal{H}}) \odot \mathbf{D}_3\mathbf{D}_1^{\mathcal{H}}, \end{aligned} \tag{69}$$

where $\mathbf{A}_{\rm d}$ denotes the columns of $\mathbf{A}$ associated with the data subcarriers ${\rm Ind}_{\rm d}$, and $\mathbf{D}_3 = \mathbf{I}_Q \otimes \mathbf{F}_P\mathbf{R}_{{\rm c},i}(\mathbf{I}_Q \otimes \mathbf{F}_P)^{\mathcal{H}}$.

REFERENCES

[1] W. Yuan *et al.*, “From ground to sky: Architectures, applications, and challenges shaping low-altitude wireless networks,” 2025. [Online]. Available: https://arxiv.org/abs/2506.12308

[2] Q. Luo *et al.*, “Toward AFDM-based scalable and secure Internet of things for low-altitude economy networks,” *IEEE Internet Things Magaz.*, pp. 1–8, 2026.

[3] D. He, W. Yuan, J. Wu, and R. Liu, “Ubiquitous UAV communication enabled low-altitude economy: Applications, techniques, and 3GPP’s efforts,” *IEEE Network*, pp. 1–1, 2025.

[4] Z. Sui *et al.*, “Multi-functional chirp signalling for next-generation multi-carrier wireless networks: Communications, sensing and ISAC perspectives,” 2025. [Online]. Available: https://arxiv.org/abs/2508.06022

[5] Q. Luo *et al.*, “Chirp-based OCDM and AFDM waveforms for 6G and beyond: Principles, recent advances, and future opportunities,” *Authorea Preprints*, 2026. [Online]. Available: https://www.authorea.com/doi/full/10.22541/au.177145233.37871971

[6] F. Liu, Y. Cui, C. Masouros, J. Xu, T. X. Han, Y. C. Eldar, and S. Buzzi, “Integrated sensing and communications: Toward dual-functional wireless networks for 6G and beyond,” *IEEE J. Sel. Areas Commun.*, vol. 40, no. 6, pp. 1728–1767, 2022.

[7] H. Yin, *et al.*, “Affine frequency division multiplexing: Extending OFDM for scenario-flexibility and resilience,” May 2025. [Online]. Available: https://arxiv.org/abs/2502.04735

[8] R. Hadani, S. Rakib, M. Tsatsanis, A. Monk, A. J. Goldsmith, A. F. Molisch, and R. Calderbank, “Orthogonal time frequency space modulation,” in *2017 WCNC*, 2017, pp. 1–6.

[9] Y. Liu, Y. L. Guan, and D. González, “Near-optimal BEM OTFS receiver with low pilot overhead for high-mobility communications,” *IEEE Trans. Commun.*, vol. 70, no. 5, pp. 3392–3406, 2022.

[10] X. Ouyang and J. Zhao, “Orthogonal chirp division multiplexing,” *IEEE Trans. Commun.*, vol. 64, no. 9, pp. 3946–3957, 2016.

[11] A. Bemani, N. Ksairi, and M. Kountouris, “Affine frequency division multiplexing for next generation wireless communications,” *IEEE Trans. Wireless Commun.*, vol. 22, no. 11, pp. 8214–8229, 2023.

[12] H. S. Rou *et al.*, “From orthogonal time–frequency space to affine frequency-division multiplexing: A comparative study of next-generation waveforms for integrated sensing and communications in doubly dispersive channels,” *IEEE Signal Proce. Mag.*, vol. 41, no. 5, 2024.

[13] A. A. Boudjelal, R. Y. Bir, and H. Arslan, “Redefining orthogonal coexistence: A mother waveform framework for DFT-based waveforms,” 2025. [Online]. Available: https://arxiv.org/abs/2503.12676

[14] K. Zheng, M. Wen, T. Mao, L. Xiao, and Z. Wang, “Channel estimation for AFDM with superimposed pilots,” *IEEE Transl Veh. Techno.*, 2024.

[15] Y. Wang, Y. He, L. Zhao, and Y. Jiang, “AFDM based preamble sequence transmission for 6G mobile satellite communication systems,” *IEEE Trans. Wireless Commun.*, 2025.

[16] K. R. R. Ranasinghe, H. Seok Rou, G. Thadeu Freitas de Abreu, T. Takahashi, and K. Ito, “Joint channel, data and radar parameter estimation for AFDM systems in doubly-dispersive channels,” *IEEE Trans. Wireless Commun.*, vol. 24, no. 2, pp. 1602–1619.

[17] Q. Luo *et al.*, “AFDM-SCMA: A promising waveform for massive connectivity over high mobility channels,” *IEEE Trans. Wireless Commun.*, vol. 23, no. 10, pp. 14 421–14 436, 2024.

[18] Y. Tao, M. Wen, Y. Ge, J. Li, E. Basar, and N. Al-Dhahir, “Affine frequency division multiplexing with index modulation: Full diversity condition, performance analysis, and low-complexity detection,” *IEEE Journal Sel. Areas Commun.*, 2025.

[19] Q. Li, J. Li, M. Wen, X. Dang, H. Arslan, and N. Al-Dhahir, “Affine frequency division multiplexing for 6G networks: Fundamentals, opportunities, and challenges,” *IEEE Network*, 2025.

[20] X. Wang, L. Xiao, Q. Luo, J. Zhou, M. Wen, and T. Jiang, “Low-complexity vector-by-vector detector for AFDM-IM systems by reconstructing sparse channel matrix,” *IEEE Commun. Lett.*, 2025.

[21] G. Xia, P. Xiao, Q. Luo, B. Ji, Y. Zhang, and H. Zhou, “Power allocation for cell-free MIMO integrated sensing and communication,” 2025. [Online]. Available: https://arxiv.org/abs/2505.19845

[22] J. Zhu *et al.*, “AFDM-based bistatic integrated sensing and communication in static scatterer environments,” *IEEE Wireless Commun. Lett.*, vol. 13, no. 8, pp. 2245–2249, 2024.

[23] K. R. R. Ranasinghe *et al.*, “Blind bistatic radar parameter estimation for AFDM systems in doubly-dispersive channels,” 2024. [Online]. Available: https://arxiv.org/abs/2407.05328

[24] Y. Ni, Z. Wang, P. Yuan, and Q. Huang, “An AFDM-based integrated sensing and communications,” in *IEEE ISWCS*, 2022, pp. 1–6.

[25] A. Bemani, N. Ksairi, and M. Kountouris, “Integrated sensing and communications with affine frequency division multiplexing,” *IEEE Wireless Commun. Lett.*, vol. 13, no. 5, pp. 1255–1259, 2024.

[26] H. S. Rou and G. T. F. de Abreu, “Normalized ambiguity function characteristics of OFDM, OTFS, AFDM, and CP-AFDM for ISAC,” *arXiv preprint arXiv:2510.11216*, 2025.

[27] H. Yin *et al.*, “Ambiguity function analysis of AFDM signals for integrated sensing and communications,” *IEEE J. Sel. Areas Commun.*, vol. 44, pp. 196–211, 2026.

[28] Y. Ni, F. Liu, H. Yin, Y. Tang, Y. Ma, and Z. Wang, “Ambiguity function analysis of AFDM under pulse-shaped random ISAC signaling,” *IEEE Trans. Wireless Commun.*, vol. 25, pp. 13 619–13 635, 2026.

[29] Y. Ni, P. Yuan, Q. Huang, F. Liu, and Z. Wang, “An integrated sensing and communications system based on affine frequency division multiplexing,” *IEEE Trans. Wireless Commu.*, vol. 24, no. 5, 2025.

[30] E. Bedeer, “Ambiguity function analysis of affine frequency division multiplexing for integrated sensing and communication,” 2025. [Online]. Available: https://arxiv.org/abs/2504.02582

[31] F. Zhang, Z. Wang, T. Mao, T. Jiao, Y. Zhuo, M. Wen, W. Xiang, S. Chen, and G. K. Karagiannidis, “AFDM-enabled integrated sensing and communication: Theoretical framework and pilot design,” 2025. [Online]. Available: https://arxiv.org/abs/2502.14203

[32] F. Xiao, Z. Li, and D. Slock, “Multipath component power delay profile based joint range and doppler estimation for AFDM-ISAC systems,” 2025. [Online]. Available: https://arxiv.org/abs/2503.10833

[33] Y. Luo, Y. L. Guan, Y. Ge, and C. Yuen, “Target sensing with off-grid sparse bayesian learning for AFDM-ISAC system,” 2025. [Online]. Available: https://arxiv.org/abs/2503.10011

[34] Y. Luo, Y. L. Guan, Y. Ge, D. González, and C. Yuen, “A novel angle-delay-doppler estimation scheme for AFDM-ISAC system in mixed near-field and far-field scenarios,” *IEEE Internet Things J.*, 2025.

[35] S. E. Zegrar, H. Haif, and H. Arslan, “OTFS-based ISAC for super-resolution range-velocity profile,” *IEEE Trans. Commun.*, vol. 72, no. 7, pp. 3934–3946, 2024.

[36] H. Pu, X. Wang, A. Kumar, L. Su, and H. Li, “OTFS-ISAC system with sub-nyquist ADC sampling rate,” *IEEE J. Sel. Areas Commun.*, vol. 44, pp. 212–228, 2026.

[37] H. Yin, X. Wei, Y. Tang, and K. Yang, “Diagonally reconstructed channel estimation for MIMO-AFDM with inter-doppler interference in doubly selective channels,” *IEEE Trans. Wireless Commun.*, vol. 23, no. 10, pp. 14 066–14 079, 2024.

[38] J. Zhu, Q. Luo, G. Chen, P. Xiao, and L. Xiao, “Design and performance analysis of index modulation empowered AFDM system,” *IEEE Wireless Commun. Lett.*, 2023.

[39] C. Komninakis, C. Fragouli, A. H. Sayed, and R. D. Wesel, “Multi-input multi-output fading channel tracking and equalization using kalman estimation,” *IEEE Trans. Signal Proce.*, vol. 50, no. 5, 2002.

[40] T. Y. Al-Naffouri, “An EM-based forward-backward kalman filter for the estimation of time-variant channels in OFDM,” *IEEE Trans. Signal Processing*, vol. 55, no. 7, pp. 3924–3930, 2007.

[41] R. Roy and T. Kailath, “ESPRIT-estimation of signal parameters via rotational invariance techniques,” *IEEE Trans. Signal Process.*, vol. 37, no. 7, pp. 984–995, 1989.

[42] A. Moussa, W. Liu, Y. D. Zhang, and M. S. Greco, “Multi-target location and doppler estimation in multistatic automotive radar applications,” *IEEE Trans. Radar Systems*, vol. 2, pp. 215–225, 2024.

[43] P. Stoica and A. Nehorai, “MUSIC, maximum likelihood, and Cramér-Rao bound,” *IEEE Trans. Acoust., Speech, Signal Process.*, vol. 37, no. 5, pp. 720–741, May 1989.

[44] Z. Li *et al.*, “Chirp parameter selection for affine frequency division multiplexing with MMSE equalization,” *IEEE Trans. Commun.*, 2024.

[45] S. E. Zegrar, H. Haif, and H. Arslan, “OTFS-based ISAC for super-resolution range-velocity profile,” *IEEE Trans. Commun.*, vol. 72, no. 7, pp. 3934–3946, 2024.

Qu Luo received the Ph.D. degree from the University of Surrey, U.K., in 2024. He is currently a Research Fellow of wireless communications with 5GIC/6GIC, Institute for Communication Systems, University of Surrey. Prior to this, he was with Huawei Technologies Company Ltd., Chengdu, China, from 2019 to 2020. He was a recipient of the Exemplary Reviewer Awards of *IEEE Wireless Communications Letters* from 2020 to 2023 and *IEEE Communications Letters* from 2022 to 2023 and the Best Paper Awards of the IEEE CSPS in 2018, the IWCMC in 2024 and the GLOBECOM in 2025. He was also a Workshop Organizer/Co-organizer for IEEE WCNC 2026, IEEE ICCC 2025, IEEE UCom 2025, IEEE SPAWC 2025, and IEEE IWSDA 2023, and a Tutorial Speaker of IEEE WCNC 2026 and IEEE IWSDA 2023. Dr. Luo is also a member of the ETSI Industry Specification Group (ISG) on Multiple Access Techniques (MAT) and serves as 3GPP delegate on RAN1 meetings from the University of Surrey. He is also an Editor of *IEEE Wireless Communications Letters*. His research interests include waveform design, integrated sensing and communication, non-orthogonal multiple access, random access, Rydberg atomic quantum receiver, deep/machine learning in the physical layer.

Zilong Liu is an Associate Professor, the 6G Lab Manager, and the 2024 Outstanding Mid-Career Researcher, in the Faculty of Science and Health, University of Essex. A Distinguished Lecturer of the IEEE Vehicular Technology Society, his research generally lies in the interplay of coding, signal processing, and communications, with a major objective of bridging theory and practice. He has widely published in quality journals such as IEEE Transactions on Information Theory and IEEE Transactions on Signal Processing. So far, he has made a series of original contributions to waveforms, sequences, and multiple access. Prior to his current post, he was with Huazhong University of Science and Technology (Bachelor, 2000-2004), Tsinghua University (MSc, 2004-2007), Nanyang Technological University Singapore (PhD and postdoc, 2008-2017), University of Melbourne (Visiting PhD, 2012), the Hong Kong University of Science and Technology (Visiting PhD, 2012), and the University of Surrey (Senior Research Fellow, 2018-2019). Details of his research can be found at: https://sites.google.com/site/zilongliu2357

Leila Musavian received her PhD degree in Telecommunications from Kings College London, UK. She is currently working as Professor at University of Essex. She was Deputy Pro-Vice-Chancellor for Research at University of Essex (2018-2020) Lecturer/senior lecturer at InfoLab21, Lancaster University (2012-2016. She is currently editor of the IEEE of IEEE Communications Surveys and Tutorials (COMST), Associate editor of IEEE Transactions on Mobile Computing, and has been editor of IEEE TRANSACTIONS OF WIRELESS COMMUNICATIONS between 2015-2020. She was the Conference Workshop Co-Chair of VTC-Spring-2020, the Wireless Communications Symposium Leading Co-Chair for IEEE ICC 2021, Montreal, Canada, conference TPC Co-Chair of IEEE CAMAD 2021, Portugal, Track 2 Lead chair of IEEE WCNC 2023 and TPC Vice-Chair of IEEE ICC 2026, Glasgow, UK. She has been the founding chair and co-chair of the IEEE UK & Ireland Future Networks Local Group. Her research interests lie in physical layer design for 6G, Doppler Resilient Modulation and Waveform, performance analysis, energy efficiency and cross-layer design for delay QoS provisioning, RIS, NFC, Massive MIMO, Energy Harvesting and SWIPT.

Nikolaos Thomos is currently a Professor at the University of Essex, U.K. Before that, he was a Senior Researcher at the Ecole Polytechnique Federale de Lausanne (EPFL) and the University of Bern, Switzerland. He received the Diploma (MSc equivalent) and Ph.D. degrees from the Aristotle University of Thessaloniki, Greece. He has been PI and co-I for a number of ESPRC, SNSF, EC, InnovateUK, and Hassler foundation-funded projects. His research interests include machine learning for communications, multimedia communications, semantic communications, design of new waveforms, cross-layer optimization, network coding, information-centric networking, source and channel coding, and signal processing. He is an elected member of the IEEE MMSP Technical Committee (MMSP-TC) for the period 2019-2024. He received the highly esteemed Ambizione Career Award from the Swiss National Science Foundation (SNSF).

Qihao Peng received the Ph.D. degree from the School of Electronic Engineering and Computer Science, Queen Mary University of London, U.K., in 2024. He is currently a Research Fellow with the School of Electrical Engineering and Computer Science, University of Surrey, UK. His research interests include reconfigurable intelligent surface, cell-free massive MIMO, URLLC, and Rydberg atomic quantum receiver. He serves as an Associate Editor for IEEE Transactions on Communications and IEEE Wireless Communications Letters, as a Lead Guest Editor for IEEE Internet of Things Journal and IEEE Network. He also serves/served as a Co-Chair/ TPC member for a number of conferences.

Pei Xiao is a Professor in Wireless Communications in the Institute for Communication Systems (ICS) at University of Surrey. He is currently the technical manager of 5GIC/6GIC, leading the research team in the new physical layer work area, and coordinating/supervising research activities across all the work areas (https://www.surrey.ac.uk/institute-communication-systems/5g-6g-innovation-centre). Prior to this, he worked at Newcastle University and Queen's University Belfast. He also held positions at Nokia Networks in Finland. He has published extensively in the fields of communication theory, RF and antenna design, signal processing for wireless communications, and is an inventor on over 15 recent patents addressing bottleneck problems in 5G/6G systems.